공학박사 학위논문

Study on Zonal Flow: Its In-Out Asymmetry and Residual Level

Zonal Flow에 대한 연구: 이의 안쪽과 바깥쪽 간 비대칭성 및 잔여값

2020 년 2월

서울대학교 대학원
에너지시스템공학부
조 영 우

Abstract

Study on Zonal Flow: Its In-Out Asymmetry and Residual Level

Y.W. Cho

Department of Nuclear Engineering,

Seoul National University, Seoul 08826, Republic of Korea

This thesis addresses the studies on the zonal flow which is symmetric in the azimuthal direction and does not induce radial transport but suppresses the turbulent transport in tokamak plasmas. I investigate the zonal flow in two ways: 1) turbulence suppression and 2) residual level in the absence of the collision and turbulence. In-out asymmetry of ion temperature gradient (ITG) turbulence and zonal flow shear driven turbulence suppression are analyzed by performing nonlinear gyrokinetic simulation using gyroKinetic Plasma Simulation Program (gKPSP). Analysis based on $E \times B$ shear decorrelation theory well explains the simulation results and find that asymmetry of $E \times B$ flow shear makes turbulence relatively symmetric. In-out asymmetry of $E \times B$ flow shear and turbulence in KSTAR plasma is also discussed using the ECEI(Electron Cyclotron Emission Image) data. Finally, I identify the role of non-Maxwellian energetic ions on residual zonal flow via the systematic procedure using gyrokinetics and bounce-kinetics.

Keywords: Tokamak Plasma, Zonal flow, in-out asymmetry, energetic ions, Gyrokinetics, ECEI

Student Number: 2013-23184

Contents

I. INTRODUCTION

In tokamak plasma, there's $E \times B$ flow which runs in binormal direction, and is symmetric in toroidal and poloidal direction but oscillates in the radial direction. Based on its origin, $E \times B$ flow is classified into mean $E \times B$ flow and zonal flow. Mean $E \times B$ flow comes from the radial electric field calculated from the radial force balance equation. Thus, it does not linearly damped and evolves when radial profiles of plasma flow and pressure change. Whereas, zonal flow is driven by turbulent Reynolds stress which is generated by drift wave instabilities excited by free energy sources such as the radial gradient of particle density and temperature, and Maxwell's stress driven by the fluctuation of magnetic fields. It is linearly damped in collisionless plasma, but not completely and saturates to a certain level. This undamped level is called residual zonal flow level which is firstly derived using gyrokinetic theory[1].

Both mean $E \times B$ flow and zonal flow play a crucial role in suppression of turbulent transport and thus enhance the confinement time, which is the reason why they have been received attention in a tokamak plasma. Based on the two-point correlation theory, the mechanism and specific criteria of the flow-shear-induced turbulence suppression were analytically proposed in Refs. 2 and 3. Besides, it is confirmed by most plasma turbulence simulations with the zonal flow, which shows the significant reduction of the turbulence eddy size and intensity, resulting in the reduction of transport-level to the gyroBohm scale. In the experiments, the mean radial electric field identified via radial force balance equation shows the correlation with the formation of transport barriers, like internal transport barrier (ITB)

and edge transport barrier (ETB). Besides, L-H transition was observed when externally imposed biased voltage, which establishes the radial electric field, exceeds the threshold. 2D wave spectrum analysis showed the suppression of the fluctuations which corresponds to the analytic results that turbulence is reduced when $E \times B$ shearing rate exceeds turbulence autocorrelation rate.

For flute-like fluctuations, $E \times B$ shearing rate ω_E has following form[3]:

$$\omega_E = \frac{\Delta\psi}{\Delta\phi}\frac{\partial^2}{\partial\psi^2}\phi_{00}(\psi) = \frac{\Delta r}{r\Delta\Theta}\frac{(RB_\theta)^2}{B}\frac{\partial^2}{\partial\psi^2}\phi_{00}(\psi) \tag{1}$$

where $\Delta r = \Delta\psi/RB_\theta$ and $R\Delta\phi$ are the correlation lengths of the ambient turbulence in the radial, and toroidal direction, respectively. And ϕ_{00} is the electric potential symmetric in toroidal and poloidal direction. Usually, correlation length in the binormal direction $r\Delta\Theta$ is assumed to be the same as the radial correlation length Δr. Note that it was derived based on the kinetic theory which can calculate the perturbed electric potential generally using Poisson equation. Accordingly, the charged particles are affected by $E \times B$ drift only, not by flow motion itself and diamagnetic drift. Thus, it is $E \times B$ flow shear, not the shear of plasma fluid motion which suppresses the turbulence.

From Eq. (1), $E \times B$ shearing rate is not axisymmetric even though electric potential is axisymmetric and thus, $\partial\phi_{00}/\partial\psi$ is constant in toroidal and poloidal direction. This is because of the inhomogeneous magnetic field structure, which is the function of the poloidal angle in toroidal geometry. As a result, $E \times B$ shearing rate is proportional to R^3 in circular flux surface when shaping effects based on Grad-Shafranov equation are considered[3]. Meanwhile, the drift wave turbulence is also expected to

be stronger at the low field side (LFS) of the tokamak due to the unfavorable curvature of the magnetic field lines concerning the interchange drive. Therefore, both the linear growth rate of the fluctuation and the suppression by $E \times B$ flow shear are stronger at the LFS than the high field side (HFS), resulting in the reduction of in-out asymmetry of the fluctuation.

Not only the suppression of the turbulence via zonal flows, its generation and damping are also important. Until mid of the '90s, researches based on gyrofluid formalism showed that zonal flow is expected to be completely damped even in the collisionless plasma. However, M.N. Rosenbluth and F.L. Hinton analytically derived that the zonal flow in toroidal plasma is not damped in the collisionless plasma, based on gyrokinetics[1]. When simulations cannot reproduce this residual zonal flow level, they overpredict the transport level. I explain the brief mechanism of energy loss and the existence of a residual level. Zonal flow and geodesic acoustic mode are linear coupled because of the transit magnetic pumping via poloidally varying magnetic field structure in a toroidal plasma. Although orbits of the particles are radially fixed when they do bounce/transit motion, there's radial motion and thus interact with the non-zonal mode, like geodesic acoustic mode (GAM). Unlike zonal flow, other modes easily lose energy via Landau damping. So, the energy transferred by this linear coupling is completely damped. This phenomenon is seen as GAM oscillation in most of the simulations on residual zonal flow. Nevertheless, there's no radial transport of the particles, and axisymmetric density perturbations are still maintained. As a result, axisymmetric electric potential remains

but is shielded via bounce/transit particles. The analytic expression of the residual zonal flow level (R_{ZF}) contains this physics and has the following form:

$$R_{ZF} = \frac{\phi_{00}(t=0)}{\phi_{00}(t \to \infty)} = \frac{n_{cl}}{n_{cl} + n_{nc}} \tag{2}$$

Here, n_{cl} is the classical polarization density, comes from the gyroangle-dependent part of electric potential. And n_{nc} is the neoclassical polarization density that comes from the bounce/transit angle-dependent part of electric potential.

From the above explanations, I can find that the particle's motion in the normal direction to the flux surface plays a crucial role in the residual zonal flow level. Meanwhile, there are growing interests of the energetic particles, as a tokamak device becomes bigger and the plasma confinement gets enhanced. It is expected that energetic particles like fusion product α particles and particles injected by neutral beam injection (NBI) affect the residual zonal flow since they have large motions in the normal direction. But the Maxwellian distribution is not suitable to describe these particles and the slowing-down distribution should be used.

In this thesis, I address the following subjects in the remaining parts. In chapter II, I describe the in-out asymmetry of the $E \times B$ flow shear. This chapter contains the theoretic derivation of the poloidal angle dependency of $E \times B$ shearing rate and its effects on turbulence reduction via gyrokinetic simulation using gKPSP (gyroKinetic Plasma Simulation Program). I found that poloidally asymmetric $E \times B$ flow shear makes turbulence relatively symmetric in poloidal direction. In chapter 3, I address the analysis of this in-out asymmetry in the KSTAR experiments

using ECEI (Electron Cyclotron Emission Imaging) data. Since I can get the fluctuation data from 24(perpendicular to radial) $\times$ 8 (radial) channels at the same time with the time resolution as $2\mu s$, $E \times B$ velocity can be estimated using correlation analysis. Using this $E \times B$ velocity and flux surface profile from EFIT, in-out asymmetry of $E \times B$ shearing rate is calculated. Also, characteristics of the fluctuations at both LFS and HFS are analyzed. In chapter 4, I present the effect of the energetic ions on the residual zonal flow level in the systematic procedure. The orbit motions of the particles are fully addressed using the general expressions of the eikonal factors. I found that residual zonal flow level in the long wavelength regime is the same as the expressions in Ref. 1 for any isotropic distributions. Also, the enhancement of the residual zonal flow level by energetic ions are discussed. I conclude my thesis paper in chapter 5 by summarizing my researches.

II. IN-OUT ASYMMETRY OF ZONAL FLOW SHEAR AND TURBULENCE REDUCTION

In the tokamak plasma, drift wave turbulence which is driven by free energy source like temperature and density gradient induces anomalous transport across the magnetic field line. The drift wave turbulence tends to be stronger at the low field side of the torus from theory[4] because of the unfavorable curvature of the magnetic field lines with respect to the interchange mode at this side. This has been confirmed from simulations[5].

Although it is not frequently addressed, poloidal asymmetry of turbulence properties has been also observed in various devices. These include fluctuations of electron temperature, electron density and electrostatic potential in TEXT-U(Texas Experimental Tokamak-Upgrade),[6–8] amplitude and radial correlation length of density fluctuations in T-10,[9] and density fluctuation amplitude in Tore-Supra.[10] Turbulence in spherical torus exhibits even stronger in-out asymmetry than those in tokamaks.[11, 12]

Meanwhile, reduction of in-out asymmetry of fluctuations was observed during the L-H transition. After L-H transition in CCT(Continuous Current Tokamak), root mean square fluctuation level measured by reflectometer showed significant reduction at low field side, while its level at high field side remained almost at the same level, resulting in significant reduction of in-out asymmetry.[13] In DIII-D L-mode plasma, turbulent region measured by X-mode reflectometry was broader in radius at low field side. However, after the H-mode transition, the turbulent region at low field side became narrower to the level comparable to the turbulent

region at high field side.[14] A plausible explanation was the in-out asymmetry in the $\boldsymbol{E} \times \boldsymbol{B}$ shearing rate in toroidal geometry from the mean $\boldsymbol{E} \times \boldsymbol{B}$ flow.[3]

There has been steady progress in understanding tokamak turbulence through gyrokinetic simulations and now it is widely accepted that self-generated zonal $\boldsymbol{E}\times\boldsymbol{B}$ flows play a crucial role in regulating and saturating the turbulence.[15] While in-out asymmetry of turbulence is visible from various simulations,[5] there has been no systematic and theoretical studies on it in the presence of zonal flows.

In this chapter, I investigate the in-out asymmetry of ITG(Ion Temperature Gradient) turbulence and its dependence on zonal flows in a quantitative manner. I note that the electrostatic potential associated with the self-generated zonal flows is a flux function with no poloidal and toroidal dependences in most cases. Even with this flux-function potential, zonal flow shear has a significant poloidal dependence from its dependence on the nonuniform magnetic field in tokamaks as I will explain in detail in the main text. For this analysis, I use `gKPSP`(GyroKinetic Plasma Simulation Program), which is a global δf gyrokinetic PIC(particle-in-cell) code.[16] In-out asymmetry of ITG turbulence is investigated in terms of radial correlation length and turbulence amplitude.

The rest of this chapter is organized as follows. In Sec. II. A, I briefly introduce the simulation model for `gKPSP`. Poloidal dependence of $\boldsymbol{E} \times \boldsymbol{B}$ shearing rate in circular flux surface is calculated in Sec. II. B. In this section, I also show the radial profile and time evolution of turbulence intensity and zonal flow with respect to the different collisionalities. From

the characteristics that are analyzed in previous sections, in Sec. II. C, I show how in-out asymmetry of turbulence gets affected by zonal flow shear which has poloidal dependence. Conclusions are drawn in Sec. II. D.

II.A. Gyrokinetic Simulation of Ion Temperature Gradient Turbulence

II.A.1. Introduction of gKPSP

I perform ITG turbulence simulations using a global δf gyrokinetic PIC(Particle-In-Cell) code, `gKPSP`[16]. The `gKPSP` code solves the electrostatic gyrokinetic Vlasov-Poisson equations[17] including a linearized Coulomb collision operator[18] with the adiabatic electron response. I briefly introduce the gyrokinetic equation before explaining `gKPSP` code in detail.

In the plasma confined by strong magnetic field, Lorentz force makes charged particles gyrate along the magnetic field lines. Since gyration period is independent of the particles' velocity and shorter than the turbulence time scale, utilization of the gyromotion in formulating the governing equation doesn't have much effect in describing turbulence. Furthermore, Hamiltonian becomes symmetric to the gyroangle θ, so that its canonical momentum $\mu = mv_\perp^2/2$ is constant in time. So μ is the adiabatic invariant and θ becomes ignorable variable in this system.

Gyrokinetic equation is the 5D Vlasov equation which uses the above characteristics of the system. In modern gyrokinetic theory, gyrokinetic

equation is formulated using Lie transform perturbation approach. Lie transform method is recursive phase transform via extending the function in n-dimension differential geometry in terms of canonical variables and satisfies the Poisson bracket. Thus push-forward transform and pull-back transform are symmetric, and systematic calculation of the perturbed Hamiltonian and distributions is valid.

Based on the modern gyrokinetic formalism, electrostatic gyrokinetic equation is

$$\frac{\partial}{\partial t} f + \frac{d\mathbf{z}}{dt} \cdot \nabla_{\mathbf{z}} f = C(f) \tag{3}$$

Here $\mathbf{z} = (x, \theta, \varphi, v_{||})$ represents the phase space coordinate and $C(f)$ is the collision operator. $d\mathbf{z}/dt$ are determined by the Poisson bracket, such that [57]

$$\frac{d\mathbf{z}}{dt} = \{\mathbf{z}, H\}_{\mathbf{z}} = \frac{\partial z}{\partial q_i}\frac{\partial H}{\partial p_i} - \frac{\partial z}{\partial p_i}\frac{\partial H}{\partial q_i}, \tag{4}$$

where p_i is the canonical momentum of q_i. And Hamiltonian in the electrostatic limit is

$$H(\mathbf{z}) = \frac{|\mathbf{p}|^2}{2m} + e\phi = \frac{1}{2} m v_{\|}^2 + \frac{\mu^2}{2m} + e\phi. \tag{5}$$

At the each time step, gyrokinetic simulation solves Eq. (3) and then calculate the Gauss equation to find ϕ in the simulation domain.

In the δf-scheme, only the perturbed part of distribution function δf evolves in time as

$$\frac{\partial}{\partial t}\delta f + (\dot{\mathbf{z}}_0 + \dot{\mathbf{z}}_1)\cdot\nabla_{\mathbf{z}}\delta f = -\dot{\mathbf{z}}_1\cdot\nabla_{\mathbf{z}} f_0 + C(\delta f, f_0) + C(f_0, \delta f) - \gamma_s \delta f + S_{cor}(\mathbf{z}, t) + S_H(\mathbf{z}, t). \tag{6}$$

A magnetic flux surface label $x = \sqrt{\psi/\psi_{edge}}$ is used as the radial variable, where ψ is equilibrium poloidal magnetic flux. $\dot{\mathbf{z}}_0$ and $\dot{\mathbf{z}}_1$ denote the unperturbed and perturbed motion of gyro-center, respectively. $C(\delta f, f_0)$ and $C(f_0, \delta f)$ represent the test particle and field particle component of the linearized Coulomb collision operator, respectively. The numerical method in Ref. 19 is used for PIC simulation of the collision operator.

A modified Krook operator $-\gamma_s \delta f + S_{cor}$ is employed to control discrete particle noise in the simulations. Since the original Krook operator damps the noise and physical fluctuations simultaneously, the correction term S_{cor} is needed to prevent artificial damping of physical quantities, especially the axisymmetric quantities related to zonal flow [20]. The correction operator S_{cor} is chosen as

$$S_{cor}(\mathbf{z}, t) = \sum_{i=1}^{N} g_i(s,t) M_i(\mathbf{z}) f_0(\mathbf{z}). \tag{7}$$

The parameters $g_i(s,t)$ can be set to conserve a set of physical quantities M_i. In this model, the three conserved quantities are chosen: zonal flow structure $M_1 = v_{||}/B - \langle v_{||}/B \rangle_\Psi$, the density $M_2 = 1$, and the kinetic energy $M_3 = v^2$. Here, $\langle \cdots \rangle_\Psi$ represents the bounce orbit average[20]. Although f_0 is time independent, turbulence-driven transport relaxes the temperature profile via perturbed quantities. For steady state simulation, profile control is necessary. To this end, a heat source S_H is implemented as

$$S_H(\mathbf{z}, t) = -\gamma_H(x) \left[\delta f(\mathbf{z}, t) - f_0(\mathbf{z}) \frac{\delta n(x,t)}{n_0(x)} \right], \tag{8}$$

where n_0 and δn correspond to the equilibrium and perturbed density, respectively. This heat source continuously damps the components of

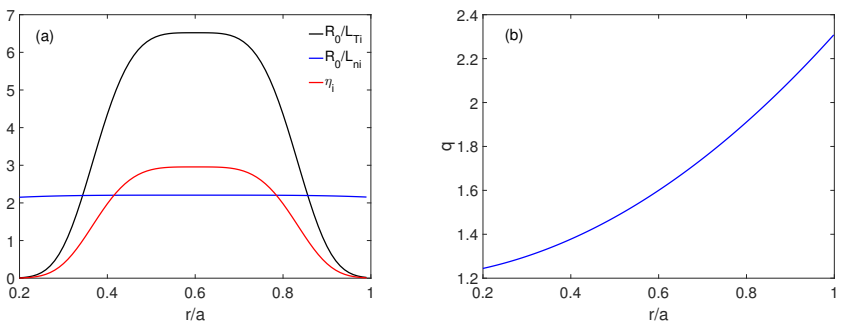

FIG. 1: Initial profiles of (a)R_0/L_{Ti}, R_0/L_{ni}, $\eta_i = L_{ni}/L_{Ti}$, and (b) safety factor q.

the perturbed distribution δf deviating from the equilibrium distribution f_0 on a time scale $1/\gamma_H$. So, the heat source drives the temperature profile toward the initial equilibrium form, and do not modify the zonal component of density fluctuations.

The growth of non-axisymmetric fluctuations is reduced by applying the modified Krook and heating operator as $\gamma_L \to \gamma_L - \gamma_s - \gamma_H$. Relaxation rate γ_s and heating/cooling parameter γ_H are set to be sufficiently smaller than both the linear growth rate $\gamma_L \simeq 0.35 v_{Ti0}/R_0$ and the inverse of turbulence correlation time $1/\tau_c \simeq 0.1 v_{Ti0}/R_0$, i.e., $\gamma_s = \gamma_H \sim \gamma_L/20$. (Here, R_0 and $v_{Ti0} = \sqrt{T_{i0}/m_i}$ are the major radius and the ion thermal velocity in the center of plasma, respectively.) So, the effects of the noise and profile controls on turbulence evolution are limited.

I use a concentric circular equilibrium of deuterium plasma with $R_0 = 210cm$ and the minor radius $a = 70cm$. The radial profile of ion temperature gradient is given by $R_0/L_{Ti} = 6.67 \exp(-y_T^4)$, where $y_T = (r - r_m)/(0.25a)$ and $r_m = 0.6a$. The electron temperature profile is

set as the same with T_i. The density gradient profile is flat and given by $R_0/L_{ni} = 2.22\exp(-y_n^4)$, where $y_n = (r - r_m)/a$. These gradient profiles as well as $\eta_i = L_{ni}/L_{Ti}$ are shown in Fig. 1 (a). The radial profile of safety factor q, which is plotted in Fig. 1 (b), has a parabolic shape with $q = 1.6$ and magnetic shear $s = 0.5$ at $r = r_m$. The ion temperature and the normalized ion gyroradius are $T_i(r = 0) = T_{i0} = 4.5keV$ and $\rho_{i0}/a \approx 1/140$ in the center, respectively. The size of radial grid is set as $\Delta r \approx 0.7\rho_{i0}$. The range of toroidal mode number is chosen as $[-64, 64]$, for which $|k_\theta \rho_i| \leq 1.0$ at the center of the unstable region ($r/a = 0.6$). I use about 100 marker particles per grid.

II.B. Collisionality dependence of turbulence and zonal flow

Before analyzing the simulation results, I illustrate the $E \times B$ shearing rate and its poloidal dependency in the circular flux surface used in this simulations. In toroidal geometry, the $\boldsymbol{E} \times \boldsymbol{B}$ shearing rate for flute-like fluctuations has following form[3]

$$\omega_E = \frac{\Delta\psi}{\Delta\varphi}\frac{\partial^2}{\partial\psi^2}\Phi_{00}(\psi) = \frac{RB_\theta \Delta r}{\nu\Delta\Theta}\frac{\partial^2}{\partial\psi^2}\Phi_{00}(\psi) = \frac{\Delta r}{r\Delta\Theta}\frac{(RB_\theta)^2}{B}\frac{\partial^2}{\partial\psi^2}\Phi_{00}(\psi), \tag{9}$$

where $\Delta\psi = RB_\theta\Delta r$, $\Delta\varphi = \nu\Delta\Theta$, ν is the local safety factor, and Φ_{00} is the zonal component of potential fluctuation. Δr and $\Delta\Theta$ are the radial correlation length and poloidal correlation angle of the turbulence eddy, respectively. In most cases, turbulence eddy is assumed to be circular, so that $\Delta r \sim r\Delta\Theta$. Using this assumption, Eq. (9) becomes

$$\omega_E = \frac{(RB_\theta)^2}{B}\frac{\partial^2}{\partial\psi^2}\Phi_{00}(\psi). \tag{10}$$

In my model, the magnetic field is expressed as $\boldsymbol{B} = I\nabla\varphi + \nabla\varphi \times \nabla\psi$ where φ is the toroidal angle and $I = B_0 R_0$ with the magnetic field in the center B_0. This leads toroidal magnetic field $B_\phi = I/R$ and poloidal magnetic field $B_\theta = |\nabla\psi|/R$. For concentric circular flux surfaces, most gyrokinetic codes including gKPSP set ψ as

$$\frac{d\psi}{dr} = \frac{I\epsilon}{q(r)\sqrt{1-\epsilon^2}}, \tag{11}$$

where $\epsilon \equiv r/R_0$. Therefore, there is no poloidal dependency in $|\nabla\psi|$, and I can rewrite the $\boldsymbol{E} \times \boldsymbol{B}$ shearing rate as

$$\omega_E(r,\theta) = \frac{R}{I}\left|\nabla\psi\right|^2 \frac{\partial^2}{\partial\psi^2}\Phi_{00}(\psi) = \frac{R_0(1+\epsilon\cos\theta)}{I}\left|\nabla\psi\right|^2 \frac{\partial^2}{\partial\psi^2}\Phi_{00}(\psi) \tag{12}$$

This results in the $\boldsymbol{E} \times \boldsymbol{B}$ shearing rate proportional to R. Meanwhile, when ψ satisfies Grad-Shafranov equation, $\omega_E \propto R^3$[3] which has stronger dependency than this simulation. So, I expect that the in-out asymmetry of zonal flow shear could be more pronounced in actual experiments than my simulations. To represent the poloidal variation of the $\boldsymbol{E} \times \boldsymbol{B}$ shear, I define the local mean $\boldsymbol{E} \times \boldsymbol{B}$ shearing rate as

$$\omega_{E,rms}(\theta) = \sqrt{\int dV \omega_E^2(r,\theta') \Big/ \int dV}, \tag{13}$$

where $\int dV = \int_{r_1}^{r_2}\int_{\theta-\Delta\theta}^{\theta+\Delta\theta}\oint rR_0(1+\epsilon\cos\theta')drd\theta'd\varphi$, i.e., the average is taken around a poloidal angle θ.

To obtain different levels of zonal flow in a self-consistent manner, I vary ion density so that linear growth rate of ITG doesn't change but linear collisional damping differs the zonal flow [21]. Here, ion-ion collisionality is $\nu_{*i} \equiv \epsilon^{-3/2}\nu_{ii}qR_0/v_{Ti}$, where ν_{ii} and q are the ion-ion collision frequency and the safety factor, respectively. Furthermore, I artificially

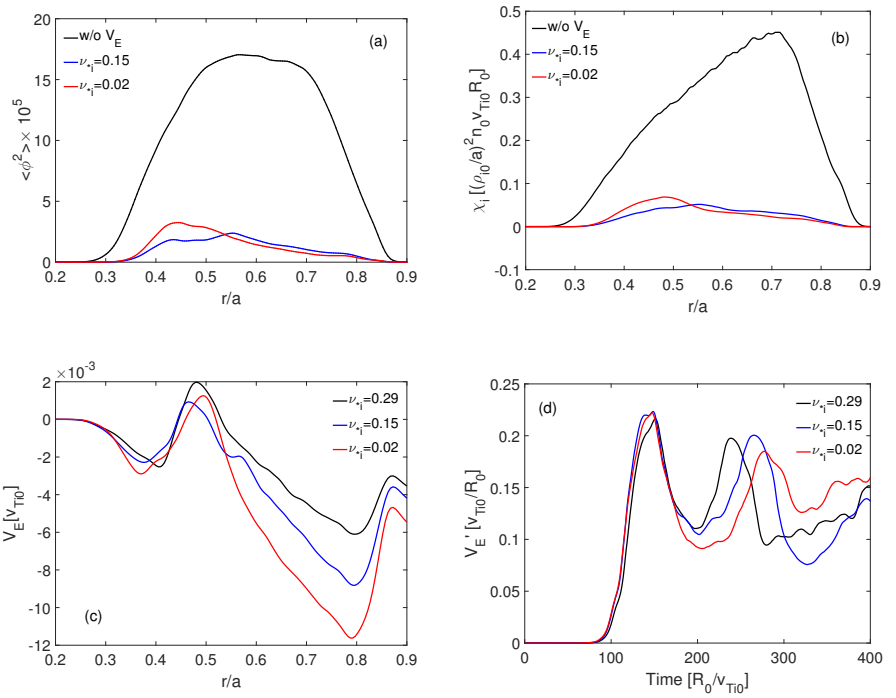

FIG. 2: Radial profiles of (a) turbulence intensity $\langle\phi^2\rangle$, (b) turbulent heat diffusivity χ_i, and (c) zonal flow V_E. And (d) time evolution of zonal flow shear V_E' integrated over volume from $r/a = 0.5$ to 0.8 for different collisionalities.

switch off the zonal flow in some runs to distinguish the effects of zonal flow from other saturation mechanisms, such as nonlinear mode coupling. The turbulence in the case without zonal flow is expected to preserve the ballooning features better. The profiles of turbulence intensity and zonal flow for the different collisionalities are shown in Fig. 2. The profiles are averaged over a steady state time period from $t/(R_0/v_{Ti0}) = 280$ to 320. In the absence of zonal flow, the shape of the turbulence intensity profile $\langle\phi^2\rangle$ in Fig. 2(a) is very similar to the R_0/L_{Ti} profile. Here, $\phi \equiv e\Phi/T_{i0}$

is the flux surface average of the normalized potential fluctuation. While turbulence intensity is almost constant in the linearly unstable region from $r/a = 0.4$ to 0.8, the radial profile of heat diffusivity shows a variation [Fig. 2(b)]. When zonal flow is retained, both turbulence intensity and turbulent heat diffusivity get reduced. The radial profiles of zonal flow are shown in Fig. 2(c). The level of zonal flow and thus its shear decrease as the collisionality increases. The strong zonal flow shear appears around $r/a = 0.6$ where the linear drive is the strongest, and turbulence reduction around $r/a = 0.6$ is more noticeable. I study characteristics of turbulence in the radial range from $r/a = 0.5$ to 0.8 in detail where the collisionality dependence of the zonal flow is clearly observed.

It is noteworthy that the collisionality dependence of the zonal flow does not persist as intended during the whole simulation period. This is because of the self-regulation dynamics between turbulence and zonal flow, which can be characterized by a 'predator-prey' model [22, 23]. The time evolution of the volume-integrated zonal flow shear, defined as

$$V_E' = \sqrt{\oint dV \omega_E^2(r,\theta) \Big/ \oint dV}, \tag{14}$$

is shown in Fig. 2(d). Here, the integration is performed in the whole domain of toroidal angle and poloidal angle and from $r/a = 0.5$ to 0.8 in radial direction. Since not only the fixed point of the predator-prey oscillation but also the oscillation amplitude depend on the zonal flow damping rate, higher collisionality does not lead to a lower level of zonal flow for the whole simulation duration. The details of the analysis based on a predator-prey model are presented in the Appendix. To avoid the complications due to the self-regulation dynamics, I analyze turbulence

properties in the time period from $t/(R_0/v_{Ti0}) = 280$ to 320 when the zonal flow level decreases with the collisionality. This time period is sufficiently longer than the turbulence correlation time $\tau_c \lesssim 10R_0/v_{Ti0}$ which will be discussed shortly.

II.C. Poloidal Asymmetry of Turbulence and Zonal Flow Shear

The radial correlation length and intensity of the ambient turbulence are significantly reduced when the $\boldsymbol{E} \times \boldsymbol{B}$ shearing rate ω_E exceeds the ambient turbulent decorrelation rate $\Delta\omega_T$, that is $\omega_E > \Delta\omega_T$ [2, 15, 22, 24–26]. I note that all the quantities have poloidal angle dependent and are larger at the low field side of the toroidal geometry. The reduction is easily measured and more pronounced for turbulence intensity from simulations. In this section, I examine the turbulence intensity and radial correlation length to investigate the poloidal dependency of the turbulence suppression by the zonal flow from `gKPSP` simulations.

First, I study the poloidal dependence of the turbulence radial correlation length and correlation time for the different zonal flow shear in a quantitative way. To evaluate the ambient turbulent scattering rate $\Delta\omega_T$, I approximate its inverse as the turbulence correlation time in the case without zonal flow. A Lagrangian time correlation function $C(\tau)$ is calculated as

$$C(\tau) = \frac{\int \phi(\mathbf{x}, t)\phi^*(\mathbf{x}, t+\tau)dV}{\sqrt{\int |\phi(\mathbf{x}, t)|^2 dV \int |\phi(\mathbf{x}, t+\tau)|^2 dV}}. \tag{15}$$

Here, $\mathbf{x} = (r, \theta)$ and τ are, respectively, a position of a turbulence eddy on a poloidal plane and the time difference. This correlation function is

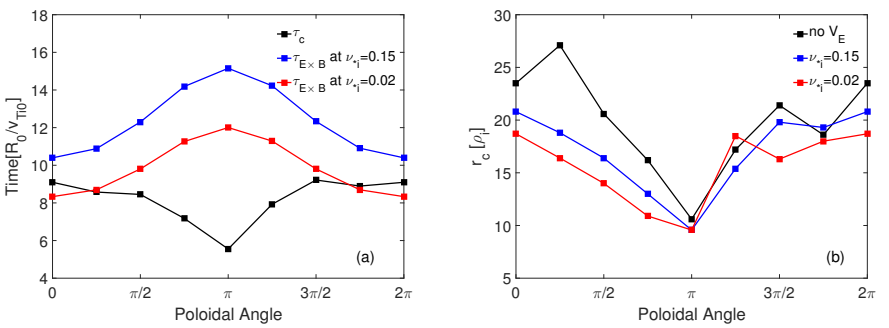

FIG. 3: (a) Turbulence correlation time τ_c, $\boldsymbol{E}\times\boldsymbol{B}$ decorrelation time $\tau_{E\times B}$, and (b) radial correlation length of turbulence as functions of poloidal angle for the different collisionalities. Local averages are taken in the range from $r/a = 0.5$ to 0.8 and $\Delta\theta = \pi/8$.

fitted by a function with a form $f_c(\tau) = \cos(\omega_0\tau)\exp[-(\tau/\tau_c)^2]$, and consequently the turbulence correlation time τ_c is obtained. Here, ω_0 is a characteristic frequency. Comparison between the turbulence correlation time τ_c and the $E\times B$ decorrelation time $\tau_{E\times B} \equiv 1/\omega_{E,rms}$ as functions of poloidal angle for different collisonalities are shown in Fig 3(a). A local average is taken from $r/a = 0.5$ to 0.8 and $\Delta\theta = \pi/8$. τ_c is the shortest at high field side(HFS) and the longest near low field side(LFS). Whereas, $\tau_{E\times B}$ shows the opposite trend. Thus the criteria for the effective reduction of the ambient turbulence, $\tau_{E\times B} < \tau_c$, is satisfied only around LFS for low collisionality.

The poloidal variations of the radial correlation length for different collisionalities are displayed in Fig. 3(b). Here, ρ_i is evaluated at LFS in the center of the radial domain ($r/a = 0.6$). At LFS, radial correlation length gets reduced in the low collisionality case since the criterion of

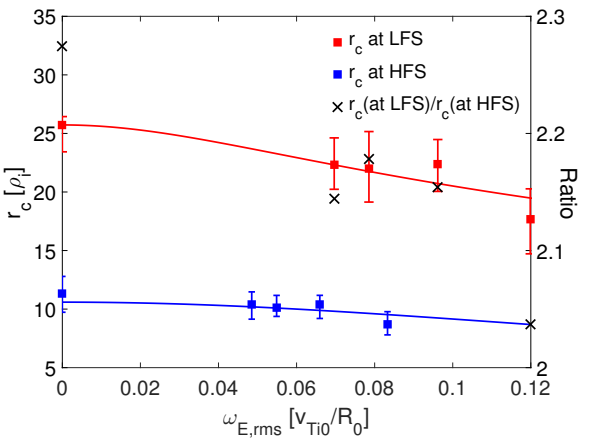

FIG. 4: Radial correlation length at LFS and HFS as a function of zonal flow shear. Black symbols show the ratio of radial correlation length at LFS to that at HFS. Solid line s are the fitted results using the $\boldsymbol{E}\times\boldsymbol{B}$ decorrelation formula in Eq. (16).

$\tau_{E\times B} < \tau_c$ is satisfied. On the other hand, the radial correlation length at HFS shows little difference for the different collisionalities because $\tau_{E\times B}$ at HFS is considerably longer than τ_c even in the low collisionality case. Consequently, the poloidal asymmetry of radial correlation length decreases as zonal flow shear increases. The poloidal asymmetry of zonal flow shear reduces the poloidal asymmetry of the turbulence correlation length.

I plot the radial correlation length as a function of the local zonal flow shear at LFS ($\theta = 0$) and HFS ($\theta = \pi$) in Fig. 4 and compare this simulation result with the analytic prediction in Refs. 24 and 25. The stronger reduction of the correlation length at LFS than that at HFS is noticeable. The ratio of radial correlation length at LFS to that at HFS

is also plotted in Fig. 4. (The zonal flow shear is taken from the values at LFS.) As the zonal flow shear increases, the in-out asymmetry of the correlation length gradually decreases. According to Refs. 24 and 25, the radial correlation length gets reduced according to the following equation when $\boldsymbol{E} \times \boldsymbol{B}$ shear is not too strong

$$r_c = \frac{r_{c0}}{(1 + \tau_c^2 \omega_{sE}^2)^{1/2}}, \tag{16}$$

where τ_c and r_{c0} are the correlation time and radial correlation length of ambient turbulence. To consider the eddy shape dependence of zonal flow shear [27], I define $\omega_{sE} = \Delta r \omega_E / r \Delta\Theta \approx r_c \omega_E / r_{c0}$. The poloidal correlation length is assumed to be same as the radial correlation length in the case without zonal flow. The reduction of the radial correlation length as a function of zonal flow shear is well fitted by the analytic formula if I use the turbulence correlation time $\tau_c = 9.5$ at LFS and $\tau_c = 5.8$ at HFS. The values of the correlation time measured from my simulations are $\tau_c = 9.1$ at LFS and $\tau_c = 5.6$ as shown in Fig. 3(a), in a good agreement with the values used for fitting the theoretical formula.

Next, I examine the poloidal asymmetry of the local mean potential fluctuation intensity ϕ^2 for different collisionalities and plot in Fig. 5(a). The local average is taken in the same range of the correlation analysis (from $r/a = 0.5$ to 0.8 and $\Delta\theta = \pi/8$). The turbulence intensity is significantly reduced by the presence of the zonal flow for the whole poloidal angle. This can be understood in terms of the nonlinear energy transfer from turbulence to zonal flow, leading to the conservation of the total energy [22]. In contrast to the turbulence decorrelation process, this turbulence energy transfer process is not localized in the LFS as shown in Fig.

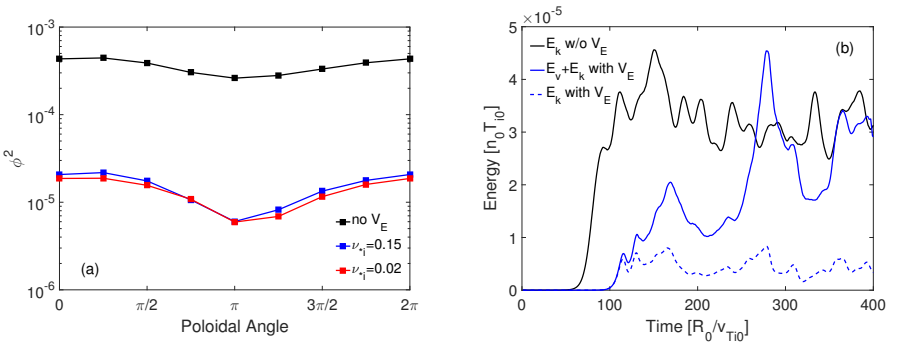

FIG. 5: (a) Local mean turbulence intensity ϕ^2 as a function of poloidal angle. (b) Time histories of the zonal flow E_v and turbulence energy E_k in the cases with, and without zonal flow. In the case with zonal flow, $\nu_{*i} = 0.02$.

5(a). The total energy of turbulence and zonal flow can be approximately expressed as[28]

$$E_{tot} = E_v + E_k = \int dV \frac{m_i n_0(r)}{2} V_E^2(r) + \int dV \frac{n_0(r) T_i(r)}{2} \sum_{m,n} (1 + k_\perp^2 \rho_s^2) \phi_{mn}^2. \tag{17}$$

Here, E_v and E_k denote the energies of the zonal flow and the turbulence, respectively. The integration is performed in the whole 3D simulation domain. The time histories of the turbulence energy in the case without zonal flow and the total energy in the case retaining zonal flow with $\nu_{*i} = 0.02$ are displayed in Fig. 5(b). In this calculation of the turbulence energy, I neglect the small term related to the polarization drift for simplicity. The total energy of zonal flow and turbulence becomes comparable to the turbulence energy excited without zonal flow after an initial transient phase. In the case with zonal flow, the turbulence energy corresponds 13% of the total energy during the time period from $t/(R_0/v_{Ti0}) = 280$ to 320. Al-

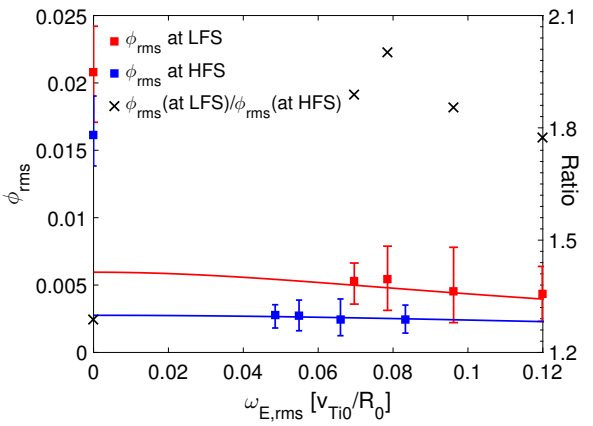

FIG. 6: Local mean turbulence amplitude ϕ_{rms} as a function of zonal flow shear. Error bar indicates the range of ϕ_{rms} variation measured from $t/(R_0/v_{Ti0}) =$ 280 to 320. Black symbols represent the ratio of ϕ_{rms} at LFS to that at HFS. Solid lines are the fitted results using an $\boldsymbol{E} \times \boldsymbol{B}$ decorrelation formula.

ternatively, about 87% of the turbulence energy is nonlinearly transferred to zonal flow in the simulations.

The turbulence amplitude ϕ_{rms} is represented as a function of zonal flow shear at LFS and HFS in Fig. 6. The ratio of turbulence amplitude at LFS to that at HFS plotted in this figure summarizes the behavior of the in-out asymmetry of the amplitude. Compared to the case without zonal flow, the presence of zonal flow enhances the in-out asymmetry of the turbulence amplitude. The in-out asymmetry of the amplitude $\phi_{rms,LFS}/\phi_{rms,HFS}$ is 1.3 in the case without zonal flow, and increases to 1.7-2.0 with zonal flow. This significant enhancement of the in-out asymmetry of turbulence amplitude is different from the modest and gradual

decrease in the in-out asymmetry of the radial correlation length. On the other hand, for non-zero zonal flow, the in-out asymmetry of the amplitude peaks at a certain level of zonal flow shear and then decreases slightly as zonal flow shear becomes stronger.

A formula describing the turbulence level reduction by $\boldsymbol{E} \times \boldsymbol{B}$ shear decorrelation, without considering the effects of nonlinear energy transfer explicitly, can be obtained by adopting a mixing length relation (i.e., $\phi \propto r_c$).[24] The resulting formula has the identical form to the equation for the radial correlation length reduction in Eq. (16), that is $\phi_{rms} \propto 1/(1 + \tau_c^2 \omega_{sE}^2)^{1/2}$. The results fitting the cases with zonal flow are presented in Fig. 6. The amplitude reduction trends in the cases with zonal flow are well described by the turbulence decorrelation theory at LFS and HFS. However, the ambient turbulence amplitude obtained by this fitting to the $\boldsymbol{E} \times \boldsymbol{B}$ decorrelation theory is much smaller than that measured in the simulation excluding zonal flow.

Now, I illustrate the different behaviors of turbulence amplitude and radial correlation length in the following fashion. ϕ_{rms} as a function of r_c is shown in Fig. 7. A noticeable feature is the difference in the amplitude to correlation length ratio ϕ_{rms}/r_c (i.e., the slope of lines in Fig. 7) between simulations with and without zonal flows. I speculate that this can result from the difference in the dominant nonlinear saturation mechanisms between the two cases. In the absence of zonal flow, the stationary turbulence properties are determined by the balance between the turbulent energy transfer via nonlinear couplings involving both strongly ballooning and flute-like modes, and the linear drive. In the presence of

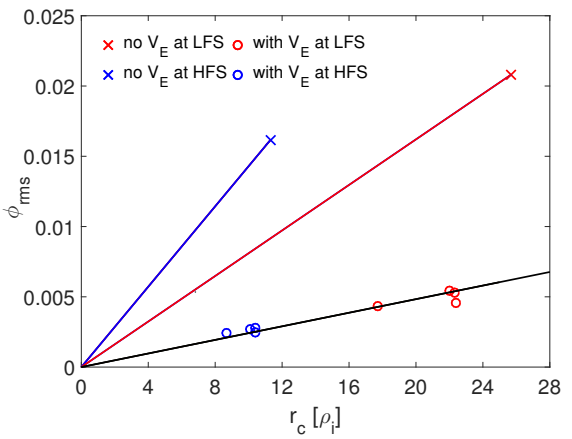

FIG. 7: Turbulence amplitude ϕ_{rms} as a function of the radial correlation length r_c. The ratios of the amplitude to the length ϕ_{rms}/r_c can be classified into three values, which correspond the slopes of three lines. The black line fits the values at both LFS and HFS in the cases with zonal flow. The other two lines fit the values at LFS and HFS in the case without zonal flow, respectively.

zonal flow, on the other hand, the nonlinear energy transfer to zonal flow is the dominant turbulence saturation mechanism, as illustrated in Figs. 5(a) and (b). So, the qualitatively different saturation mechanisms could lead to different amplitude to length ratio values.

In addition to the properties of potential fluctuation, I briefly report the in-out asymmetry of the ion heat transport. Turbulent heat diffusivity χ_i at LFS and HFS as well as their ratio are shown in Fig. 8. Compared to the case without zonal flow, the presence of zonal flow significantly reduces χ_i at both LFS and HFS and decreases its in-out asymmetry. Among the cases retaining zonal flow, in-out asymmetry of χ_i increases with zonal

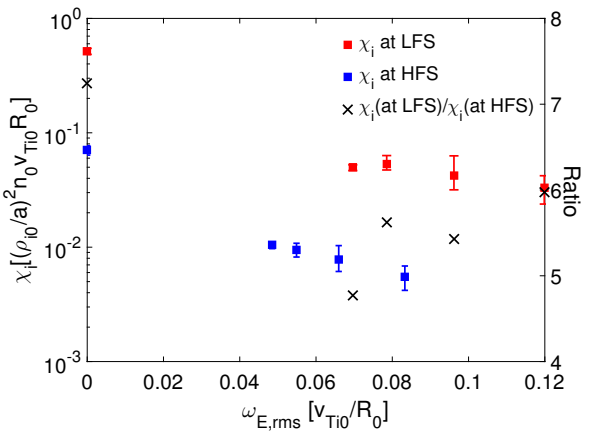

FIG. 8: Turbulent heat diffusivity χ_i as a function of zonal flow shear. Error bar indicates the range of χ_i variation measured from $t/(R_0/v_{Ti0}) = 280$ to 320. Black symbols represent the ratio of χ_i at LFS to that at HFS.

flow shear. The reduction of the χ_i magnitude with the increased zonal flow (shear), or equivalently, with low collisionalities is similar to the behavior of the turbulence intensity in my simulations. But the behavior of the in-out asymmetry of χ_i is opposite to that of the turbulence amplitude. To elucidate the behavior of the in-out asymmetry of χ_i, detailed analysis of ion temperature fluctuation δT_i is necessary but has not been performed in this work. I defer a study of the in-out asymmetry of the heat transport in a subsequent paper.

II.D. Conclusions

I have investigated the poloidal asymmetry of ITG turbulence in toroidal geometry for different zonal flow levels. I have performed gyroki-

netic simulations and analyzed the turbulence amplitude, radial correlation length, and correlation time of the potential fluctuations as functions of the poloidal angle. To clarify the effect of zonal flow, the fluctuation characteristics in the presence of zonal flow are compared to those in the simulation without zonal flow. It is found that the in-out asymmetry of the radial correlation length continuously decreases as zonal flow shear increases because the reduction of the correlation length is larger at LFS than HFS. This correlation length reduction trend from the zero zonal flow case is well described by the $\boldsymbol{E} \times \boldsymbol{B}$ shear decorrelation theory. However, turbulence amplitude behaves differently from the prediction of the mixing length relation in combination with the decorrelation theory [24]. It seems that while the $\boldsymbol{E} \times \boldsymbol{B}$ decorrelation theory works well for the radial correlation length, more detailed nonlinear theory taking nonlinear energy transfer from turbulence to zonal flow into account rather than a naive mixing length relation is required to predict the behavior of turbulence amplitude.

III. ANALYSIS OF IN-OUT ASYMMETRY OF $E \times B$ FLOW SHEAR USING ECEI DATA

In this section, I extend my previous gyrokinetic study on the in-out asymmetry of $E \times B$ flow shear to the experiments. Unlike the simulations, it is difficult to analyze the problem in limited situations like electrostatic ITG turbulence with an adiabatic electron case. In addition, the mean radial electric field E_r can be estimated using radial force balance equation, but the zonal flow is almost unmeasurable. Meanwhile, correlation analysis via ECEI data[31] makes it possible to distinguish the fluctuations of each mode. Furthermore, $E \times B$ flow velocity can be derived from the wave velocity of the modes. One of the advantages of the analysis using ECEI is that radial profiles of the plasma pressure, binormal flow velocity, and magnetic field strength are not necessary to calculate the E_r. Thus, from this research, I can verify my research on in-out asymmetry of the $E \times B$ shearing rate in the gyrokinetic simulation, through the KSTAR experiments.

For these reasons, I analyze the in-out asymmetry of $E \times B$ flow shear in the KSTAR experiments measured by ECEI. The remained part of this section is organized as follows. In the Sec. III. A.1., I briefly introduce the experiment I analyzed. Then, I compare the velocity of the fluctuations estimated by ECEI data and $v_{E\times B}$ deduced from the CES data on radial profiles of T_i and v_T in the Sec. III. A.2. And finally, I analyze the effects of the $E \times B$ shearing rate on the in-out asymmetry of the fluctuations measured by ECEI in Sec. III A.3. In Sec. III B., I address the summary and the future work for this topic.

III.A. Analysis of Poloidal Asymmetry of the Fluctuations and $E \times B$ shearing rate

III.A.1. Set-up of the Experiments

In order to analyze the in-out asymmetry of the fluctuations and the $E \times B$ shearing rate, I investigate the previous KSTAR experiments in which ECEI system measured both the low field side (LFS) and the high field side (HFS) at the same time. One of the past experiments which fulfill this condition is the KSTAR #18431. In this experiment, plasma was heated by three neutral beam (NB) injection channels with their power 1.7, 1.08, and $1.7MW$. Toroidal magnetic field strength on-axis was $2.3T$, and the plasma current was on the reversed direction with $500kA$. Ion temperature and toroidal velocity were measured by CES from $t = 6s$ to $t = 9s$. Based on the measured data, equilibrium magnetic surface, and radial profiles of T_i, v_T, and safety factor q are calculated using EFIT code.

Time evolution of total energy, electron density, β, Z_{surf}, and plasma elongation κ are illustrated in Fig. 9. Here, Z_{surf} is the flux-surface-averaged vertical location of the last closed flux surface. In this H-mode plasma with type-1 ELM, bursty $n = 2$ fishbone mode and weak $n = 1$ harmonic oscillation at the core was observed by Mirnov coil from $t = 5.5s$ to $6.15s$. From $t = 6s$, the external magnetic field pushed the plasma down, so that β_p decreased with Z_{surf} slowly moving down. Plasma was extremely destabilized after $t = 8s$, because of the disruption. Although this experiment is not suitable to analyze because of this external mag-

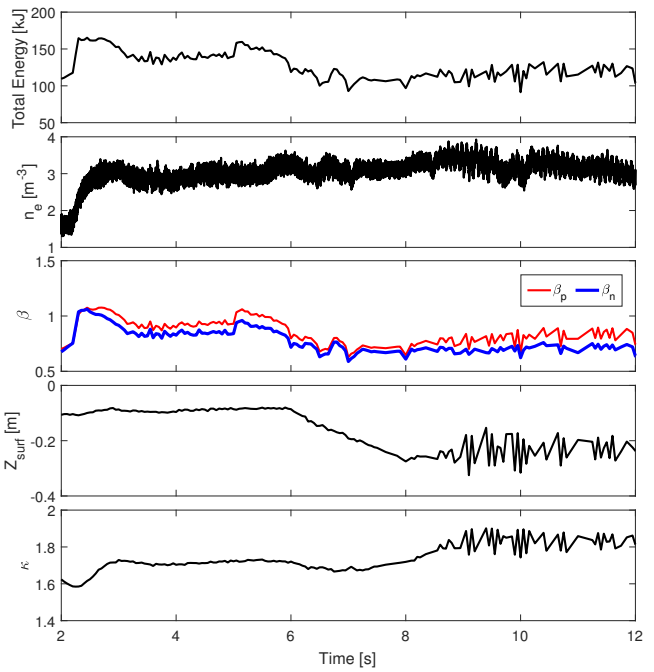

FIG. 9: Time evolution of the total energy, electron density, β, Z_{surf}, and plasma elongations at KSTAR #18431. Plasma moved down from $t = 6s$ and stopped at $t = 8s$. Plasma was measured by CES from $t = 6s$ and stopped at $t = 9s$

netic field, it is one of the few experiments which was observed using CES and ECEI at both LFS and HFS. In addition, MHD modes have a stronger spectrum compared to other fluctuations, which can lead to higher accuracy in this analysis. Due to the above reasons, I analyze the KSTAR experiment #18431 from $t = 6s$ to $t = 6.1s$, when there's both CES data and ECEI data and MHD phenomenon occurred.

In order to analyze the in-out asymmetry of $E \times B$ shearing rate on the same flux surface, I illustrate the equilibrium magnetic flux surface from

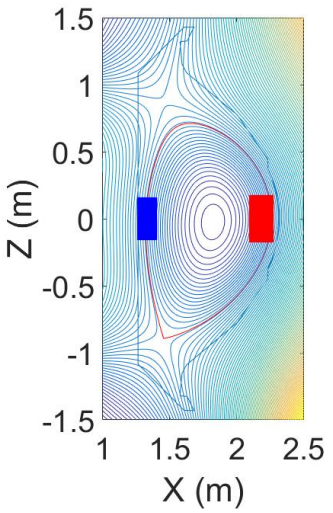

FIG. 10: Magnetic flux surface calculated by ECEI at $t = 6s$. Red and blue box correspond to the location where ECEI measured. Red line is the last closed flux surface.

EFIT and the position where ECEI detected in Fig. 10. ECEI detected the plasma inside the last closed flux surface (LCFS) at the LFS, whereas it detected the plasma across the LCFS at the HFS. Thus, I analyzed the spectrum from the channels which detected inside the LCFS.

III.A.2. Estimation of the $E \times B$ shearing rate

In most cases, radial electric field E_r from the experimental data is estimated using radial force balance equation[27]. To calculate the E_r using radial force balance equation, I need the radial profiles of pressure, toroidal rotation speed, and poloidal rotation speed. Usually, this data are measured by charge exchange spectroscopy (CES)[30]. It measures the

radiation emitted by the excited impurity ions due to the charge exchange between a neural hydrogen atom and an impurity ion[30]. Generally, a neutral hydrogen atom comes from the neutral beam injection from the outside of the tokamak. So this spectroscopy requires the device to inject the neutral beam source.

Whereas, Electron Cyclotron Emission Imaging (ECEI) system measures the radiation emitted by the gyration of electrons in the magnetized plasmas [31]. Since the frequency of the gyration is the function of the charge, mass, and magnetic field, the location of the emission can be estimated based on the magnetic field strength. So, ECEI measures the intensity of the radiation emitted by the gyromotion and estimate the electron temperature fluctuations.

If $E \times B$ shearing rate can be estimated using ECEI, this detection system can give us not only the information of the fluctuation of T_e, but also the current status of the stabilization effects. The main method to estimate $E \times B$ velocity is the correlation analysis using the signals from the multi-channels. Comparing the two signals with the same frequency of nearby channels, the phase difference between two channels can be measured. Using phase difference $\Delta\theta$ and distance between the channels Δd, I can find the wavelength $k = \Delta\theta/\Delta d$ with respect to the frequency of the signal[32]. Since $E \times B$ flow induces the Doppler shift of the wave frequency,

$$\omega_{Th} = \omega_{Lab} - k_\theta v_{E\times B} \tag{18}$$

where ω_{Th} is the actual frequency of the wave, ω_{Lab} is the measured frequency, and k_θ is the wavelength measured by the phase difference between

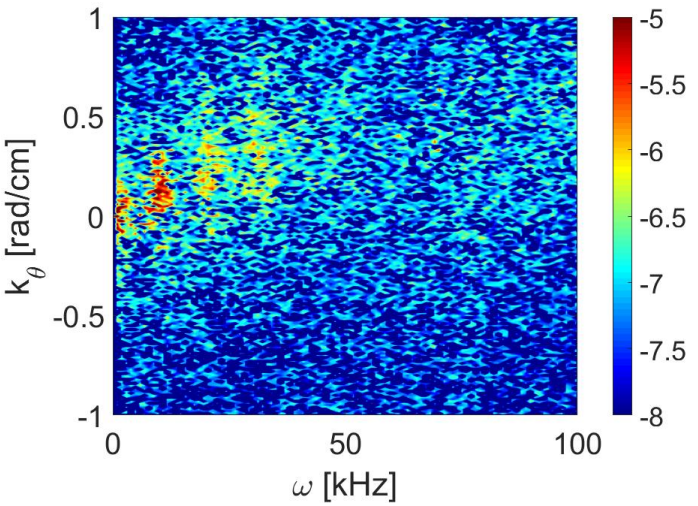

FIG. 11: Spectrum of the $\langle \tilde{T}/T \rangle$ on wavelength and frequency at the LFS.

the two channels[33]. So, phase velocity measured in the lab frame is the function of the phase velocity in the plasma frame and $E \times B$ velocity.

Fig. 11 shows the spectrum of the T_e fluctuation calculated from the ECEI data. Spectrum at the LFS shows the poloidal flow motion of the fluctuation induced by the Doppler shift due to the $E \times B$ flow. Since this flow motion is not merely due to the $E \times B$ flow, the assumption on the plasma phase velocity and group velocity are needed. Moreover, the phase velocity is difficult to identify when the amplitude of the fluctuation is weak. So I calculate the group velocity using RANdom SAmple Consensus (RANSAC) method[34] for higher reliability. This numerical method aims to distinguish the inlier data from the outlier data by random sampling. I commit the random sampling with weighting each data by the $S(k, \omega)$. Then, the trend of the sampled data is deduced and check the consensus to the other data which is not selected by random sampling. After repeating

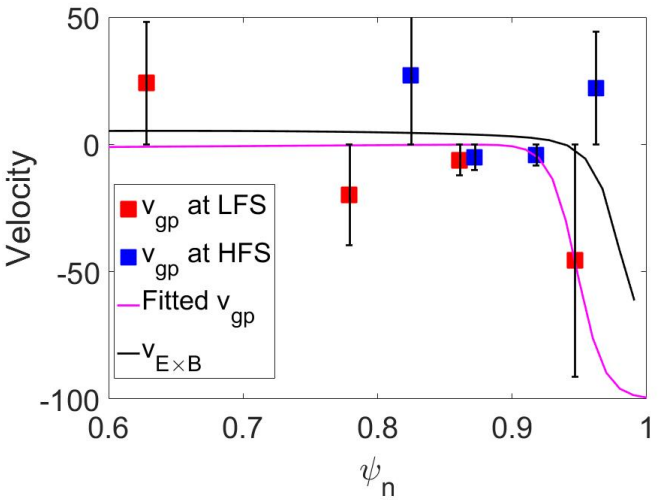

FIG. 12: Group velocity v_{gp} deduced from the fluctuations measured by ECEI and $v_{E\times B}$ calculated using radial profiles of the T_i and v_T measured by CES. Purple line is the fitted using v_{gp} and Eq. 20.

this process several times, I choose the trend which has the least outlier and determines the group velocity of the fluctuations.

The radial electric field E_r is deduced from the radial force balance equation using CES data. But there's only CES data on ion temperature T_i and toroidal velocity v_T in this experiment which is the reason why few assumptions for the profiles that were not measured are used. For the pressure profile, I assume that $T_e(r) = T_i(r)$ and $n_i(r)/n_{i0} = T_i(r)/T_{i0}$. Poloidal velocity is deduced from the neoclassical poloidal velocity. Consequently, the equation of $v_{E\times B}$ in this work is

$$v_{E\times B} \simeq \frac{E_r}{B_T} = \frac{1}{B_T}\left(v_T B_\theta - v_{\theta Neo} B_T + \frac{1}{n_i Z e}\nabla P\right) \tag{19}$$

Comparisons on the $E\times B$ velocity ($v_{E\times B}$) and the group velocity (v_{gp})

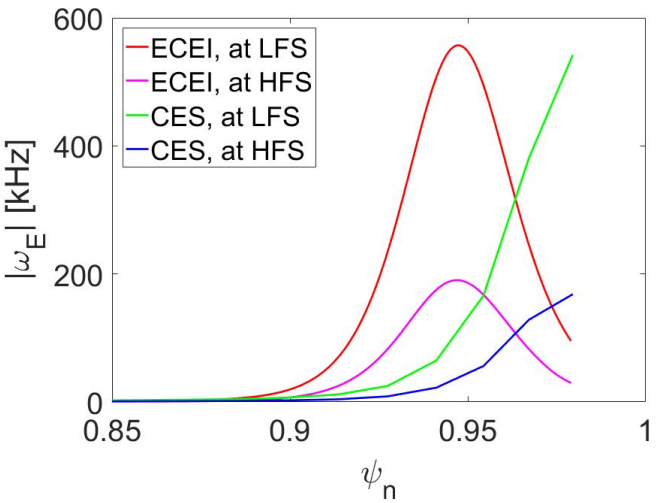

FIG. 13: $|\omega_E|$ deduced from the ECEI data and CES data at the both LFS and HFS.

of the fluctuations are illustrated in Fig. 12. v_{gp} at the LFS and that at the HFS are comparable, which corresponds to the characteristics of the $v_{E\times B}$ which is independent of the poloidal angle. To compare v_{gp} with $v_{E\times B}$ and their shear, I use the following equation to fit the v_{gp}.

$$v_{gp} = A_1 \frac{(1 + b\Delta\psi_n)exp(\Delta\psi_n) - exp(-\Delta\psi_n)}{exp(\Delta\psi_n) - exp(-\Delta\psi_n)} + A_2 \tag{20}$$

Here, $\Delta\psi_n = (\psi_n - \psi_n(r_{TB}))/\Delta_b$, r_{TB} is the location of transport barrier, and Δ_b is the width of transport barrier. Fitted v_{gp} is slower than $v_{E\times B}$, but their radial tendencies are similar. Also, the measured radial location of the transport barrier is different between the $v_{E\times B}$ and v_{gp}, which is due to the measurement position error of the two measurement devices.

To calculate ω_E, I assume that Doppler shift by the $v_{E\times B}$ has a dominant role on the radial variation of the v_{gp}. ω_E in Fig. 13. is calculated

by

$$\omega_E = \frac{1}{B_T}|\nabla\psi|^2 \frac{\partial}{\partial\psi}\left(\frac{B_T}{|\nabla\psi|}v_{E\times B}\right) \tag{21}$$

As mentioned in the previous paragraph, there's a difference in the position of the $max(|\omega_E|)$ resulting from the ECEI and CES. It is also reflected in the asymmetry of ω_E since this asymmetry is the function of R. The ratio of the $max(|\omega_E|)$ between that at the LFS and HFS is 3.22 and 2.93 for the data measured by CES and ECEI, respectively.' ω_E is proportional to $(R^{2.1})$, which has stronger poloidal asymmetry than the results in the gyrokinetic simulation at the concentric circular flux surface ($\propto R^1$)[35]. The main reason for the strong poloidal asymmetry compared to the simulation is the magnetic field structure with shaping effects. In my previous work, poloidal angle dependent part of the ω_E is the $|\nabla\psi|^2/B_T$ and $\partial^2\phi_{ZF}(\psi)/\partial\psi^2$ is independent of the poloidal angle. Actually, $|\nabla\psi|^2/B_T \propto R^{2.1}$, which is much stronger in-out asymmetry than $|\nabla\psi|^2/B_T \propto R^1$ in concentric flux surface. Therefore, shaping effect which was not considered in my previous work enhances the in-out asymmetry of ω_E.

III.A.3. Effect of ω_E on the in-out asymmetry of the fluctuations

To analyze the effect of in-out asymmetry of ω_E, I first calculate the correlation time t_c at both sides, which is shown in Fig. 14. a). The correlation time of the LFS is longer than that of the HFS only near the $\psi_n = 0.8$. To compare the t_c to the ω_E, I use the ω_E from the ECEI, since t_c is calculated using the data from ECEI. At the LFS, $E\times B$ decorrelation

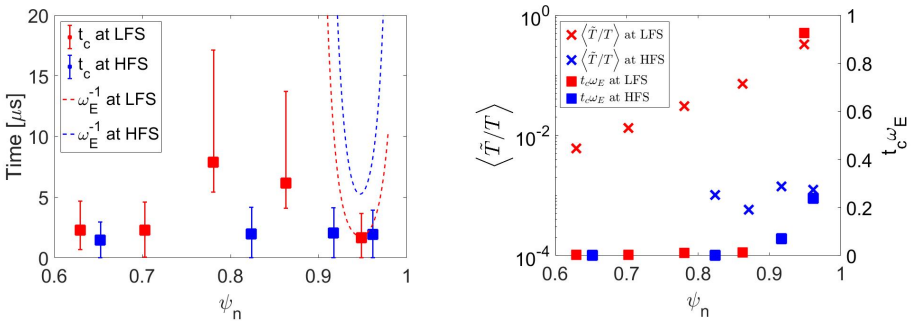

FIG. 14: a) Correlation time t_c and ω_E^{-1}, estimated using ECEI data. b) Electron temperature fluctuation $\langle \tilde{T}/T \rangle$ and $t_c\omega_E$ on the ψ_n.

time ω_E^{-1} is comparable to the t_c at the $\psi_n \in [0.9, 0.95]$, which corresponds to the location of the transport barrier. Because of the in-out asymmetry of ω_E, opposite relation is shown in the HFS. So, a weaker reduction of the turbulence at the HFS is expected. However, this estimation is not applicable to analyze the traits of temperature fluctuations $\langle \tilde{T}/T \rangle$ in Fig. 14 b). Although $t_c\omega_E \sim 1$ at the transport barrier ($\psi_n \sim 0.95$), $\langle \tilde{T}/T \rangle$ is the highest. This can be because of ELM activities and MHD instabilities, which are measured as strong fluctuations and are not stabilized by $E \times B$ flow shear. Thus, in order to figure out the role of the $E \times B$ flow shear on turbulence fluctuations, I need to restrict the range of wavelength and frequency.

III.B. Summary and Future work

In this work, I analyze the in-out asymmetry of the $E \times B$ shearing rate ω_E using the data estimated by the ECEI system. To convince the

results, I investigate the experiments which measured by both CES and ECEI the same time, in order to compare the $v_{E\times B}$ calculated by usual radial force balance equation, to the correlation analysis based on the ECEI data. Although plasma moved down at the measured time, KSTAR #18431 was one of the few experiments which were measured by the ECEI at both LFS and HFS, and CES at the same time. At first, I compare the group velocity v_{gp} estimated from the ECEI data, with the $v_{E\times B}$ calculated from the radial force balance equation using the radial profiles of the T_i and v_T measured by CES. It is shown that v_{gp} is slower than the $v_{E\times B}$ and the location of the transport barrier differ, but their shear is comparable.

In-out asymmetry of the $E \times B$ shearing rate is stronger than that at the gyrokinetic simulation in my previous research[35]. It comes from the magnetic field structure $|\nabla\psi|^2/B_T$ with shaping effects. The comparison between correlation time t_c and ω_E is consistent with the theoretic prediction on the enhancement of the confinement. Nevertheless, temperature fluctuations do not correspond to this prediction and the observation of the transport barrier because of the ELM and MHD activities.

As future work, I need more experiment results to convince my present results. First, by comparing more results on $v_{E\times B}$ using CES data and v_{gp} estimated by ECEI data, I need to ensure my calculation on ω_E. Then, from the results which observed the LFS and HFS at the same time using ECEI, in-out asymmetry of the $E \times B$ shearing rate can be estimated. Finally, the analysis of the role of the $E \times B$ flow shear on the fluctuations should be performed on the drift wave wavelength and frequency regime.

IV. RESIDUAL ZONAL FLOW IN THE PRESENCE OF THE ENERGETIC IONS

Zonal flows are well-known to regulate and reduce the tokamak plasma turbulence. A noteworthy property of zonal flows in toroidal plasma is that it is not damped to non-zero amplitude, known as residual zonal flow, in the absence of collisional and turbulence induced damping. Since Rosenbluth and Hinton analyzed residual zonal flow level in the long wavelength regime ($k_r\rho_{i,b}$, $\rho_{i,b}$ is banana orbit width) [1], there have been various extensions which mostly assumed Maxwellian equilibrium for every ion species. However, for fusion product α-particles in tokamak plasmas, the Maxwellian distribution is a poor approximation and the slowing-down distribution should be used.

In this chapter, I study the residual zonal flow level in the presence of α particles with slowing-down distribution function and compare the results against those for Maxwellian distribution case with the same average kinetic energy and the case without α particles. I only consider the electrostatic fluctuations in the limit of adiabatic electron response for simplicity in this work. Mostly, I consider a parameter regime expected for ITER core plasmas.

Principal results of this chapter are as follows. The values for n_{cl} and n_{nc} for the same dimensionless radial wave number $k_r\rho_i^T$, normalized to the average-energy ion gyroradius $\rho_i^T = \sqrt{\bar{E}/m}/\Omega_c$ are not significantly different depending on the ion equilibrium distribution function, whether it's a Maxwellian or a slowing-down in long wavelength limit. However, since typical α-particle's Larmor radius is much larger than that of back-

ground ion Larmor radius, for the zonal flows in the k_r range satisfying $k_r\rho_i^T < 1 < k_r\rho_\alpha^T$, I obtain that classical polarizability of alpha particle is significantly higher than that of background ions, with a consequence of R_{ZF} with α-particles exceeding R_{ZF} in the absence of α-particles considerably. The beneficial effect on confinement from this is predicted to depend on the α-particle's concentration. The effect is obviously negligible if n_α/n_e is negligible. However, for $n_\alpha/n_e = 10\%$ I predict more than 10% enhancement of residual zonal flows for $k_r\rho_{i,eff} \approx 10^{-1}$. I note that the predicted value of n_α/n_e in ITER depends on the operation scenarios and assumptions used in models[70, 71].

An analytic derivation is possible for an arbitrary well-behaved equilibrium distribution function F_0 for the long wavelength($k_r\rho_{\theta,i}^T \ll 1$) zonal flows. In this regime, the well-known expression for a high aspect ratio circular tokamak plasmas[1], i.e., $R_{ZF} = 1/(1+1.6q^2/\sqrt{\epsilon})$ which has been derived for Maxwellian F_0, remains to be valid for any well-behaved F_0 which is isotropic in velocity space.

The remainder of this chapter is organized in the following order. In Sec. IV.A.1, I introduce the slowing down distribution function for energetic ions. n_{cl} and n_{nc} for slowing down distribution function in arbitrary wavelength regime are derived in Sec. IV.A.2, and 3 respectively. Then, residual zonal flow level for slowing down distribution function is estimated in Sec.IV.B. and compared to the Maxwellian F_0 case. Discussions regarding other related works are given in Sec. IV.C.

IV.A. Classical and Neoclassical Polarization Density

In this section, I derive expressions for the classical and neoclassical polarization density for arbitrary wavelength. More details can be found from the following works. Wang and Hahm[53] have derived the generalized expressions which are valid for the arbitrary wavelength of zonal flows for both classical and neoclassical polarization density using the modern gyrokinetics[56, 57] and bouncekinetics[58]. Those expressions include the finite Larmor radius (FLR) effect and finite orbit width (FOW) effect. Duthoit, Brizard, and Hahm[72] have shown how to further improve the analytic approximations. In this way, both classical and neoclassical polarization density have been derived systematically. The schematic description of pull-back transformations is illustrated explicitly in Fig. 2 of Ref. 53. I don't consider the electron dynamics which can be relevant to electron temperature gradient (ETG) turbulence driven hyper fine-scale zonal flows[50–54] for simplicity.

IV.A.1. Slowing Down Distribution Function

When high energy ions which are created or injected in the plasmas are slowed down due to collisions with background ions and electrons, the slowing down distribution is a good description of an equilibrium distribution function[73]. Assuming an isotropy in velocity space, I have

$$F_{SD}(v) = \frac{n_\alpha}{4\pi v_c^3 A_2} \frac{H(v_\alpha - v)}{1 + (\frac{v}{v_c})^3} \tag{22}$$

where v_α is the maximum velocity of an energetic particle and v_c is the slowing down critical velocity related to the electron thermal velocity of background plasmas,

$$v_c^3 = 3\frac{\sqrt{\pi}}{4}\frac{m_e}{m_\alpha}Z_I v_{th,e}^3 \tag{23}$$

Here, $Z_I = m_\alpha \Sigma_i n_i (Z_i^2/m_i)/n_e$ is an effective charge which is inversely weighted by ion mass. I use the definition $v_{th,e}^2 = 2T_e/m_e$ and $v_\alpha^2 = 2E_{birth}/m_\alpha$, while $v_{th}^2 = T/m$ for other ion species such as D and T. E_{birth} is the birth energy of energetic particle. The following integrals as functions of v_α/v_c appear in my analysis,

$$A_n\left(\frac{v_\alpha}{v_c}\right) = \int_0^{v_\alpha/v_c} \frac{x^n}{1+x^3}dx \tag{24}$$

For each n, they are given by

$$A_0(a) = \frac{1}{6}\left[ln\frac{(a+1)^3}{a^3+1} + 2\sqrt{3}\left(tan^{-1}\left(\frac{2a-1}{\sqrt{3}}\right) + \frac{\pi}{6}\right)\right] \tag{25}$$

$$A_2(a) = \frac{1}{3}ln(a^3+1) \tag{26}$$

$$A_4(a) = \frac{1}{6}\left[3a^2 + ln\frac{(a+1)^3}{a^3+1} - 2\sqrt{3}\left(tan^{-1}\left(\frac{2a-1}{\sqrt{3}}\right) + \frac{\pi}{6}\right)\right] \tag{27}$$

It has been derived from a Fokker-Planck equation which considers slowing-down of high energy particles with source an ion birth velocity that has the form of $\delta-$function in particle velocity space[73]. Therefore, Eq. (22) is applicable for fusion product α particles in the future tokamak fusion plasmas such as ITER or DEMO. For high energy ions from the negative neutral beam injection(NNBI), an anisotropic distribution should be considered depending on the NBI injection direction. I need to define an effective temperature for non-Maxwellian distribution function

for proper normalizations. I take the average kinetic energy($\bar{E}$) and define the effective temperature(T_{eff}), accordingly, i.e.,

$$\bar{E} = \frac{1}{2n}\int mv^2 F_0(Z)d^3v \equiv \frac{3}{2}T_{eff} \tag{28}$$

for an arbitrary distribution function $F_0(Z)$. Here, Z denotes the guiding center coordinates. The mean kinetic energy for slowing down distribution is given as following,

$$E_{SD} = \frac{1}{2n_\alpha}\int m_\alpha v^2 F_{SD}(v)d^3v \equiv \frac{3}{2}T_{SD} = \frac{A_4}{2A_2}T_c \tag{29}$$

Then, the temperature of the equivalent Maxwellian distribution function $T_M = T_{SD}$ and the critical temperature of slowing down distribution defined as $T_c = mv_c^2$ are related by

$$T_M \;=\; \frac{A_4}{3A_2}T_c \tag{30}$$

From now on, I use the average mean kinetic energy for any distribution function for normalization of $v_{th,i}$, ρ_i^T, and ρ_θ^T, i.e., $v_{th,i} = \sqrt{T_{eff}/m}$. "$T$" will be used as a simplified notation for T_{eff} (T_{SD} for slowing-down distribution) unless specified otherwise. Also, I use v_α as the birth speed of fusion product α-particles.

IV.A.2. Classical polarization density

Classical polarization density(n_{cl}) comes from the difference between the particle density and the gyrocenter density[56, 57, 74]. Nonlinear gyrokinetic formulations[56, 57, 75] don't assume Maxwellian equilibrium distribution. Modern gyrokinetic approach[56, 57, 76] separates the polarization density systematically in the gyrokinetic Poisson equation.

For an arbitrary distribution function $F(Z)$, n_{cl} in the presence of a zonal potential $\delta\phi$ can be expressed as following[77] :

$$n_{cl} = \frac{Z|e|\delta\phi}{T}\int_0^\infty\int_{-\infty}^\infty 2\pi dv_\parallel \frac{Bd\mu}{m}\left(1 - J_0^2(k_r\rho_i)\right)\left(-\frac{T\partial}{B\partial\mu}\right)F(Z_{gy}) \quad (31)$$

where B is the magnetic field strength, $v_\parallel$ is parallel velocity, $\mu = mv_\perp^2/2B$ is guiding-center magnetic moment and Z_{gy} denotes gyrocenter phase space coordinates. Since n_{cl} depends on FLR effect strongly, I consider two asymptotic wavelength regimes, the long wavelength regime $k_r\rho_i^T \ll 1$ and the short wavelength regime $k_r\rho_i^T \gg 1$. Here, ρ_i represents each ion's Larmor radius while ρ_i^T represents the Larmor radius at the thermal velocity.

In the long wavelength regime of $k_r\rho_i^T \ll 1$, the lowest order FLR effects can be approximated by using $J_0^2(x) \simeq 1 - x^2/2$. Then, n_{cl}^{long} can be calculated by

$$\begin{aligned} n_{cl}^{long} &\simeq \frac{Z|e|\delta\phi}{T}\int_0^\infty\int_{-\infty}^\infty 2\pi dv_\parallel \frac{Bd\mu}{m}\left(\frac{1}{2}k_r^2\rho_i^2\right)\left(-\frac{T\partial}{B\partial\mu}\right)F(Z_{gy}) \quad (32)\\ &= \frac{Z|e|\delta\phi}{T}v_{th,i}^2\int_0^\infty\int_{-\infty}^\infty 2\pi dv_\parallel d\mu\frac{\partial}{\partial\mu}\left(\frac{1}{2}k_r^2\rho_i^2\right)F(Z_{gy})\\ &= (k_r\rho_i^T)^2 n_0\frac{Z|e|\delta\phi}{T}. \end{aligned}$$

Then, based on the definition

$$\frac{n_{cl}}{n_0} = \chi_{cl}\frac{Z|e|\delta\phi}{T}, \quad (33)$$

I obtain the dimensionless classical polarizability for the long wavelength

$$\chi_{cl}^{long} = (k_r\rho_i^T)^2. \quad (34)$$

This derivation shows that n_{cl} and χ_{cl} in the long wavelength limit are the same for any well-behaved distribution function, because $n = \int d^3v F(v)$

holds for any $F(Z)$. Note that the temperature dependence in Eq. (32) is absent in n_{cl}^{long}. In addition, the mathematical expressions in Eqs. (32) and (34) are identical for any well-behaved distribution function.

In the short wavelength limit of $k_r\rho_i^T \gg 1$, $x = v/v_{th,i}$ and $\theta = cos^{-1}\left(v_{||}/v\right)$ are used to facilitate the integration. Then, n_{cl} for isotropic distribution can be expressed as

$$\begin{aligned} n_{cl} &= \frac{Z|e|\delta\phi}{T} v_{th,i}^3 \int_0^\infty \int_0^\pi 2\pi x sin\theta d\theta dx \left(1 - J_0^2(k_r\rho_i^T x sin\theta)\right) \left(-\frac{\partial}{\partial x}\right) F(x) \\ &= \frac{Z|e|\delta\phi}{T} v_{th,i}^3 \int_0^\infty 2\pi x dx \left(2 - H(k_r\rho_i^T x)\right) \left(-\frac{\partial}{\partial x}\right) F(x) \end{aligned} \tag{35}$$

Here, I have defined

$$\begin{aligned} H(x) &= \int_0^\pi d\theta J_0^2(x sin\theta) sin\theta \\ &= \pi H_0(2x) J_1(2x) + (2 - \pi H_1(2x)) J_0(2x) \end{aligned} \tag{36}$$

$H_n(x)$ is the Struve H function[78]. Using the asymptotic behavior, $H(x) \simeq 1/x$ for $x \gg 1$. I obtain,

$$\begin{aligned} n_{cl}^{short} &\simeq \frac{Z|e|\delta\phi}{T} v_{th,i}^3 \int_0^\infty 2\pi dx \left(2x - \frac{1}{k_r\rho_i^T}\right) \left(-\frac{\partial}{\partial x}\right) F(x) \\ &\simeq \frac{Z|e|\delta\phi}{T} 4\pi v_{th,i}^3 \left[\int_0^\infty F dx - \frac{1}{2k_r\rho_i^T} F(0)\right] \end{aligned} \tag{37}$$

Eq. (37) shows that n_{cl} in the short wavelength limit depends on $F(x)$. Note that $\int_0^\infty F(x)dx$ is not proportional to n in general. n is proportional to $\int_0^\infty F(x)x^2dx$. In particular, n_{cl} for slowing down distribution in short wavelength limit can be written as

$$\frac{n_{cl}^{short}}{n_0} = \frac{A_4}{3A_2}\left[\frac{A_0}{A_2} - \frac{1}{2A_2 k_r \rho_c}\right] \frac{Z|e|\delta\phi}{T}, \tag{38}$$

where ρ_c is the Larmor radius at T_c and $\left(\rho_i^T/\rho_c\right)^2 = T/T_c$. Eq. (38) shows that χ_{cl} for slowing down distribution asymptotes to the $A_0A_4/3A_2^2$ as

$k_r\rho_i^T \to \infty$. This originates from $\int_0^\infty dvF(v)$ which is not proportional to $n = 4\pi\int_0^\infty dvv^2F(v)$, except for a Maxwellian $F(Z)$. On the other hand, it converges to a familiar expression "1" for a Maxwellian distribution (see the first term on the R.H.S. of Eq. (31)).

To avoid a spurious pole at $k_r\rho_i^T = v_{th,i}/2A_0v_c$ in applying Eq. (38) (which is valid for $k_r\rho_i^T \gg 1$) for a connection formula for arbitrary wavelength, I slightly modify χ_{cl}^{short} as

$$\begin{aligned}\chi_{cl}^{short} &= \frac{A_4}{3A_2}\left[\frac{A_0}{A_2} - \frac{1}{2A_2k_r\rho_c}\right] \\ &\simeq \frac{A_0A_4}{3A_2^2}\left[1 + \frac{1}{2A_0k_r\rho_c}\right]^{-1}\end{aligned} \tag{39}$$

which is also valid in the short wavelength regime up to $O(\frac{1}{k_r\rho_c})$.

Now, I construct a connection formula of χ_{cl} for slowing down distribution using Eqs. (34) and (39) by following the recipe used in Ref. 53

$$\chi_{cl} = \left\{\frac{1}{1+(k_r\rho_i^T/C_k)^2}\frac{1}{\chi_{cl}^{long}} + \frac{(k_r\rho_i^T/C_k)^2}{1+(k_r\rho_i^T/C_k)^2}\frac{1}{\chi_{cl}^{short}}\right\}^{-1} \tag{40}$$

To avoid an unphysical inflection point which can occur in connection formula, I demand a continuity in the slope at a connection point, C_k

$$\frac{\partial}{\partial(k_r\rho_i^T)}\chi_{cl}^{long} = \frac{\partial}{\partial(k_r\rho_i^T)}\chi_{cl}^{short}, \quad at \quad k_r\rho_i^T = C_k \tag{41}$$

Then Eqs. (34), (39) and (41) lead to

$$C_k = \frac{v_{th,i}}{v_c}\left(\frac{1}{4A_2}\right)^{1/3} \tag{42}$$

Without this consideration, χ_{cl} can exhibit an unphysical overshoot at $k_r\rho_i^T \sim 1$[67].

I first compare the analytic results in Eqs. (34) and (39) with the result which is numerically calculated based on Eq. (31), and is presented in Fig.

15 a). Here, $T_e = 10keV$ and ρ_i^T is the average Larmor radius of energetic α particles. Analytic results predict the behavior of χ_{cl} at long wavelength regime and asymptotic level at short wavelength limit well. However, the analytic result from a connection formula in Eq. (40) overestimates χ_{cl} at $k_r\rho_i^T \sim 1.0$. Fig. 15 b) shows the χ_{cl} for F_M and F_{SD} consisting of (100%) energetic α-particles only for illustrations, at $T_e = 10keV$ and $30keV$. I set $T_i = T_e$ for background ions for a black curve for the case without α-particles. $\rho_{i,eff} = \Sigma_a c m_a v_{Ta}/Z_a|e|B$ is the effective Larmor radius of background ions for corresponding T_e. The black curve represents χ_{cl} for both cases of thermal ions at $T_e = 10keV$ and $30keV$, since χ_{cl} for F_M

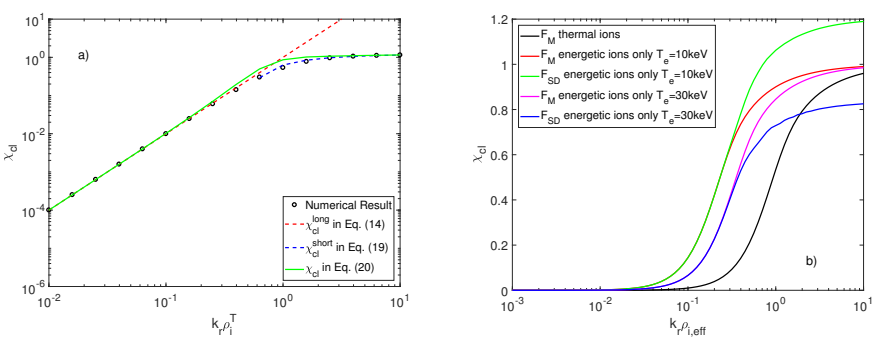

FIG. 15: a) Analytic and numerical results of χ_{cl} for F_{SD} in the wavelength range $10^{-2} \leq k_r\rho_i^T \leq 10$. Here, ρ_i^T is the Larmor radius of energetic particles. b) Numerical results of χ_{cl} based on Eq. (31) for different values of T_e and distribution function. Here, $\rho_{i,eff}$ is the effective Larmor radius of background ions for corresponding T_e and $\bar{E}_M = \bar{E}_{SD} = 814.6keV$ and $1045.5keV$ for $T_e = 10keV$ and $T_e = 30keV$, respectively. The black line represents χ_{cl} for thermal ions for $T_e = 10keV$ and $30keV$.

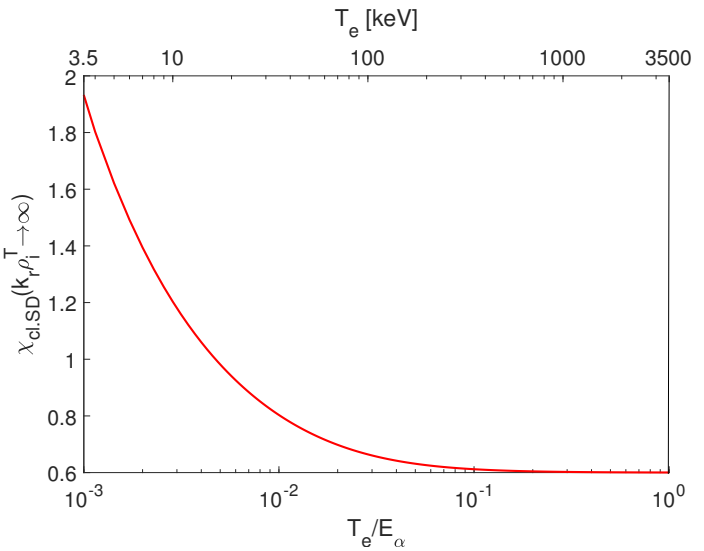

FIG. 16: Short wavelength asymptotic value of χ_{cl} for F_{SD} consisting of α-particles only for illustration as a function of T_e/E_α. Upper x-axis shows T_e when $E_\alpha = 3.5MeV$. $\chi_{cl,SD}(\infty) = 1$ for $T_e \simeq 16keV$.

is a function of $k_r\rho_i^T$. Transition to shorter wavelength regime occurs at different value of $k_r\rho_{i,eff}$. This is because of different values of Larmor radius of α-particles and of background ions with $T_i = T_e$. So, transition occurs at the same $k_r\rho_i^T$ but at different $k_r\rho_{i,eff}$.

Unlike F_M, asymptotic value of χ_{cl} for F_{SD} varies as a function of temperature in the short wavelength regime. Eq. (39) shows that this level depends on A_n which in turn depends on the v_α and v_c which is a function of electron temperature and composition of background ions. From the statistical dynamics point of view, $\partial_E lnF(E) \propto 1/k_B T_s$, where T_s is the original definition of the temperature in the this statistic dynamics. Since Maxwellian distribution is the state with the highest Entropy, no

more transport of the energy or particles occur among the phase space, temperature in terms of the statistical dynamics is the same in the phase space. Thus, asymptotic level of the χ_{cl} is always '1' for F_M. However, for non-Maxwellian distributions, if there's collision, number of particles in each energy state changes, since this T_s is different for different energy state. So, average value of the $1/k_B T_s$ can differ when internal energy of the macro state changes. I plot asymptotic level of χ_{cl} as a function of T_e/E_α in Fig. 16, where E_α is the birth energy of α-particles. As T_e gets colder, the average value of the $k_B T_s$ drops faster, resulting in the higher asymptotic level of χ_{cl}. It also means the contribution of energetic ions on χ_{cl} increases as energy of fast ions normalized to the electron temperatures increases. In particular, when $T_e/E_\alpha \lesssim 4.5 \times 10^{-3}$ ($T_e \lesssim 16keV$ for $E_\alpha = 3.5MeV$), $\chi_{cl}(k_r \rho_i \to \infty)$ exceeds 1.

IV.A.3. Neoclassical polarization density

The neoclassical polarization density(n_{nc}) is the difference between the trapped/passing particle density and the bounce/transit gyrocenter density[53, 58]. Since n_{nc} is obtained by the two step pull-back transformation (first, from bounce(transit)-center phase space to gyrocenter phase space transform, and then gyrocenter to particle phase space transform), both FOW and FLR effects should be considered[53]. So, n_{nc} should be characterized in terms of poloidal Larmor radius $\rho_{\theta i}^T$ related to the FOW effect and Larmor radius ρ_i^T related to the FLR effect.

For an isotropic distribution function in velocity space, flux surface

averaged n_{nc} can be calculated from the following expression[72] :

$$\begin{aligned} n_{nc} &= Z|e|\delta\phi\frac{B}{m}\iint 4\pi R_{||}\omega_{||}d\hat{\mu}d\hat{\kappa}\frac{\omega_{||}}{\omega_{b,t}} \\ &\times\ J_0^2(k_r\rho_i)(1-|\langle e^{i\Delta\zeta}\rangle_{b,t}|^2)\left(-\frac{\partial}{\partial E}\right)F(Z_{bgy}) \end{aligned} \tag{43}$$

Here, Z_{bgy} is the bounce-center phase space coordinate, and

$$\begin{aligned} \kappa &= \frac{E-\mu B_0(1-\epsilon)}{2\epsilon\mu B_0}, & \omega_{||} &= \frac{p_{||e}}{2\sqrt{\kappa}mR_{||}} \\ J_b &= \frac{8}{\pi}mR_{||}^2\omega_{||}[E(\kappa)-(1-\kappa)K(\kappa)], & J_t &= \frac{4}{\pi}mR_{||}^2\omega_{||}\sqrt{\kappa}E(\kappa^{-1}) \\ \omega_b &= \frac{\pi\omega_{||}}{2K(\kappa)}, & \omega_t &= \omega_{||}\frac{\pi\sqrt{\kappa}}{K(\kappa^{-1})} = \frac{\pi\omega_{||}}{K(\kappa)} \end{aligned}$$

κ is the pitch angle parameter, which is less than 1 for trapped particles and greater than 1 for passing particles. $\omega_{||}$ is the characteristic parallel frequency, $R_{||} = qR$ is the connection length and $p_{||e}$ is the equatorial parallel momentum. $J_{b,t}$ denote the second adiabatic invariant for trapped particles and passing particles, respectively. ω_b denotes bounce frequency and ω_t denotes transit frequency. $K(\kappa)$ and $E(\kappa)$ are the complete elliptic integrals of the first and second kind, respectively. Here, hats are used for the bounce-gyrocenter coordinate. From now on, I drop the hat for notational simplicity. $J_0^2(k_r\rho_i)$ indicates the FLR effect and $|\langle e^{i\Delta\zeta}\rangle_{b,t}|^2$ indicates FOW effect on n_{nc} respectively.

IV.A.4.a. Long Wavelength Regime

In long wavelength regime ($k_r\rho_i^T \ll k_r\rho_{\theta i}^T < 1$), the FLR effect can be neglected, but the FOW effect is kept to the lowest order. The orbit-

averaged eikonal factor in long wavelength limit can be expressed compactly following[72]

$$\begin{pmatrix} 1 \\ 2 \end{pmatrix} \times \frac{\omega_{||}}{\omega_{b,t}} \left(1 - |\left\langle e^{i\Delta\zeta} \right\rangle_{b,t}|^2\right) \tag{44}$$

$$\simeq \frac{\omega_{||}\alpha^2}{\omega_{b,t}} \begin{cases} \frac{E(\kappa)}{K(\kappa)} - (1-\kappa) & (0 \le \kappa < 1) \\ 2\kappa \left(\frac{E(\kappa^{-1})}{K(\kappa^{-1})} - \frac{\pi^2}{4K^2(\kappa^{-1})}\right) & (\kappa > 1), \end{cases}$$

where $\alpha = \sqrt{2\epsilon} k_r \rho_{\theta i}$. In whole regime, I use a high aspect ratio assumption for a simple expression relating energy and magnetic moment by $E = \mu B_0(1 - \epsilon + 2\epsilon\kappa) \approx \mu B_0$. Then, I can use $y = \mu B_0/T \approx E/T$.

i) n_{nc} for trapped particles:

$$\begin{aligned} n_{nc,b} &= Z|e|\delta\phi \left(\frac{T}{m^3}\right)^{1/2} \int_0^\infty \int_0^1 8\sqrt{\epsilon y} d\kappa dy \\ &\times \alpha^2 \left(E(\kappa) - (1-\kappa)K(\kappa)\right) \left(-\frac{\partial}{\partial y}\right) F(y) \\ &= 32\epsilon^{3/2} \left(k_r \rho_{\theta i}^T\right)^2 \times \frac{4}{9} \times \frac{3}{2} \langle\sqrt{y}\rangle \left(\frac{T}{m^3}\right)^{1/2} Z|e|\delta\phi \end{aligned} \tag{45}$$

Since $F(y)$ is a one dimensional distribution function, $\left\langle\sqrt{y}\right\rangle$ for arbitrary isotropic distribution is proportional to the density since

$$\begin{aligned} \langle\sqrt{y}\rangle &= \int_0^\infty y^{1/2} F(y) dy \\ &= \frac{1}{4\sqrt{2}\pi} \left(\frac{m}{T}\right)^{3/2} n_0 \end{aligned} \tag{46}$$

So, neoclassical polarization density for trapped particle in long wavelength limit becomes

$$\frac{n_{nc,b}}{n_0} \simeq 1.20\epsilon^{3/2} \left(k_r \rho_{\theta i}^T\right)^2 \frac{Z|e|\delta\phi}{T} \tag{47}$$

It means if the distribution function is isotropic in velocity space in high aspect ratio limit, n_{nc} for trapped particles in the long wavelength limit is independent of details of distribution function.

ii) n_{nc} for passing particles:

$$\begin{aligned} n_{nc,t} &= Z|e|\delta\phi \left(\frac{T}{m^3}\right)^{1/2} \int_0^\infty \int_1^\infty 8\sqrt{\epsilon y} dy d\kappa \\ &\times \alpha^2 \sqrt{\kappa} \left(E(\kappa^{-1}) - \frac{\pi^2}{4K(\kappa^{-1})}\right) \left(-\frac{\partial}{\partial y}\right) F(y) \\ &\simeq 32\epsilon^{3/2} \left(k_r \rho_{\theta i}^T\right)^2 \times 0.16 \times 1.5 \left\langle \sqrt{y} \right\rangle \left(\frac{T}{m^3}\right)^{1/2} Z|e|\delta\phi \\ &\simeq 0.43\epsilon^{3/2} \left(k_r \rho_{\theta i}^T\right)^2 n_0 \frac{Z|e|\delta\phi}{T} \end{aligned} \tag{48}$$

Note that flux surface averaged n_{nc} for passing particles in long wavelength limit is also always the same for arbitrary isotropic distribution function in high aspect ratio limit.

Therefore, n_{nc} for isotropic distribution function in long wavelength limit becomes,

$$\frac{n_{nc}}{n_0} = \frac{n_{nc,b} + n_{nc,t}}{n_0} = 1.63\epsilon^{3/2} \left(k_r \rho_{\theta i}^T\right)^2 \frac{Z|e|\delta\phi}{T} \tag{49}$$

This result is identical to that obtained by Rosenbluth and Hinton[1] for a Maxwellian distribution. Using both n_{cl} and n_{nc} in the long wavelength limit, I can recover their result by

$$R_{RH} = \frac{V_{E\times B}(t \to \infty)}{V_{E\times B}(t \to 0)} = \frac{n_{cl}}{n_{cl} + n_{nc}} = \frac{\chi_{cl}}{\chi_{cl} + \chi_{nc}} \simeq \left(1 + 1.63\frac{q^2}{\sqrt{\epsilon}}\right)^{-1} \tag{50}$$

Consequently, residual zonal flow level in the long wavelength limit is the same as the Rosenbluth-Hinton expression for *any isotropic distribution function in velocity space* in the high aspect ratio limit.

IV.A.4.b. Expression for Shorter Wavelengths

For shorter wavelength regime with $k_r\rho_{\theta i}^T \gtrsim 1$, I can use the following approximations for an eikonal factor $|\left\langle e^{i\Delta\zeta}\right\rangle_{b,t}|$ as suggested in Ref. 72.

$$|\left\langle e^{i\Delta\zeta}\right\rangle_b|^2 \simeq J_0^2(\alpha a_1(\kappa)) \tag{51}$$

$$|\left\langle e^{i\Delta\zeta}\right\rangle_t|^2 \simeq J_0^2(\alpha b_2(\kappa)) \tag{52}$$

where

$$a_1(\kappa) = 2\frac{\omega_b}{\omega_{||}} sech[0.5\pi\tau(\kappa)], \qquad \tau(\kappa) = \frac{K(1-\kappa)}{K(\kappa)}$$

$$b_2(\kappa) = \frac{\omega_t}{\omega_{||}} sech[\pi\bar{\tau}(\kappa)], \qquad \bar{\tau}(\kappa) = \frac{K(1-\kappa^{-1})}{K(\kappa^{-1})}$$

Then, Eq. (43) becomes

$$\begin{aligned} n_{nc,b} &= Z|e|\delta\phi\frac{B}{m}\iint 4\pi R_{||}\omega_{||}d\hat{\mu}d\hat{\kappa}\frac{\omega_{||}}{\omega_b} \\ &\times J_0^2(k_r\rho_i)(1-J_0^2(\alpha a_1(\kappa)))\left(-\frac{\partial}{\partial E}\right)F(Z_{bgy}) \end{aligned} \tag{53}$$

$$\begin{aligned} n_{nc,t} &= Z|e|\delta\phi\frac{B}{m}\iint 4\pi R_{||}\omega_{||}d\hat{\mu}d\hat{\kappa}\frac{\omega_{||}}{\omega_t} \\ &\times J_0^2(k_r\rho_i)(1-J_0^2(\alpha b_2(\kappa)))\left(-\frac{\partial}{\partial E}\right)F(Z_{bgy}) \end{aligned} \tag{54}$$

Then, I can numerically integrate Eqs. (53) and (54) for the slowing down distribution function and the Maxwellian distribution function. My numerical results in various figures to be presented afterwards are based on these expressions.

For thorough understanding of the results, I pursue further analytic progress by considering the intermediate wavelength regime ($k_r\rho_i^T < 1 < k_r\rho_{\theta i}^T$) and the short wavelength regime ($1 < k_r\rho_i^T < k_r\rho_{\theta i}^T$) separately in the next subsections.

IV.A.4.c. Intermediate Wavelength Regime

In the intermediate wavelength regime with $k_r\rho_i^T < 1 < k_r\rho_{\theta i}^T$, FOW effect can be considered using the approximations for eikonal factor $|\left\langle e^{i\Delta\zeta}\right\rangle_{b,t}|$ in Eqs. (51) and (52). On the other hand, FLR effects are ignored for a feasibility of constructing a connection formula in this main text. It is further discussed in the Appendix.

Then, n_{nc} for an arbitrary isotropic distribution function becomes

$$\begin{aligned} n_{nc,b/t} &= Z|e|\delta\phi\frac{B}{m}\iint 4\pi d\mu d\kappa\left(\epsilon\frac{\mu B}{m}\right)^{1/2} \\ &\times \frac{\omega_{||}}{\omega_{b/t}}(1-|\langle e^{i\Delta\zeta}\rangle_{b/t}|^2)\left(-\frac{\partial}{\partial E}\right)F(E) \\ &\simeq Z|e|\delta\phi\left(\frac{T}{m^3}\right)^{1/2}\iint 4\pi dy d\kappa\sqrt{\epsilon y} \\ &\times \left[\begin{array}{ll} \frac{\omega_{||}}{\omega_b}(1-J_0^2(\alpha a_1))\left(-\frac{\partial}{\partial y}\right)F(y) & (0\le\kappa<1) \\ 2\frac{\omega_{||}}{\omega_t}(1-J_0^2(\alpha b_2))\left(-\frac{\partial}{\partial y}\right)F(y) & (\kappa>1) \end{array}\right. \end{aligned} \tag{55}$$

For passing particles, there is a multiplicative factor of 2, because both co-passing and counter-passing particles exist. Since $\alpha a_1(\kappa) \gg 1$ and $\alpha b_2(\kappa) \gg 1$, Bessel function can be approximated as $J_0(z) \sim \sqrt{2/(\pi z)}cos(z-\pi/4)$. Using this approximation,

$$n_{nc,b} \simeq Z|e|\delta\phi\left(\frac{16\epsilon T}{m^3}\right)^{1/2}\left[\sqrt{8}\int_0^\infty F(x)dx - \frac{C_b}{\pi\sqrt{\epsilon}k_r\rho_{\theta i}^T}F(0)\right] \tag{56}$$

$$\begin{aligned} n_{nc,t} &\simeq Z|e|\delta\phi\left(\frac{16\epsilon T}{m^3}\right)^{1/2} \\ &\times \left[\sqrt{8}\left(\frac{\pi}{\sqrt{8\epsilon}}-1\right)\int_0^\infty F(x)dx - \frac{C_t}{\pi\sqrt{\epsilon}k_r\rho_{\theta i}^T}F(0)\right] \end{aligned} \tag{57}$$

Here, $x = v/v_{th,i} = \sqrt{2y}$. I define

$$C_b = \int_0^1 d\kappa \frac{K(\kappa)}{a_1(\kappa)} \simeq 3.89 \tag{58}$$

$$C_t = \int_1^\infty d\kappa \frac{K(\kappa^{-1})}{\sqrt{\kappa} b_2(\kappa)} \tag{59}$$

C_t is the function of ϵ, which becomes higher as ϵ decreases. Since $F(0)$ and the moment of v^{-2} depend on particular distribution function, a difference in n_{nc} will result accordingly. For Maxwellian distribution function, n_{nc} is expressed as

$$\frac{n_{nc,b}}{n_0} = \frac{\sqrt{8\epsilon}}{\pi}\left[1 - \frac{C_b}{2\pi\sqrt{\pi\epsilon}k_r\rho_{\theta i}^T}\right]\frac{Z|e|\delta\phi}{T} \tag{60}$$

$$\frac{n_{nc,t}}{n_0} = \frac{\sqrt{8\epsilon}}{\pi}\left[\left(\frac{\pi}{\sqrt{8\epsilon}} - 1\right) - \frac{C_t}{2\pi\sqrt{\pi\epsilon}k_r\rho_{\theta i}^T}\right]\frac{Z|e|\delta\phi}{T} \tag{61}$$

My results are somewhat different on the second term of R.H.S. when compared to those in Ref. 53. This is because of an eikonal factor I use for full finite orbit effects is valid for arbitrary pitch angle parameters of both trapped and passing particles[72] while an approximate version has been used for Ref. 53. For slowing down distribution function, contribution of trapped particles and passing particles to n_{nc} becomes

$$\frac{n_{nc,b}}{n_0} = \frac{A_0 A_4}{3A_2^2}\frac{\sqrt{8\epsilon}}{\pi}\left[1 - \frac{C_b}{\sqrt{8\epsilon}\pi A_0 k_r \rho_{\theta c}}\right]\frac{Z|e|\delta\phi}{T} \tag{62}$$

$$\frac{n_{nc,t}}{n_0} = \frac{A_0 A_4}{3A_2^2}\frac{\sqrt{8\epsilon}}{\pi}\left[\left(\frac{\pi}{\sqrt{8\epsilon}} - 1\right) - \frac{C_t}{\sqrt{8\epsilon}\pi A_0 k_r \rho_{\theta c}}\right]\frac{Z|e|\delta\phi}{T}, \tag{63}$$

where $\rho_{\theta c} = \rho_{\theta i}^T v_c / v_{th,i}$ is the ion poloidal Larmor radius at T_c. Note that asymptotic value of χ_{nc} in this wavelength regime for slowing down distribution function differs from that for Maxwellian distribution by $A_0 A_4 / 3A_2^2$, i.e. by the same factor for the χ_{cl} in the short wavelength regime.

IV.A.4.d. Short Wavelength Regime

In the short wavelength limit where $1 < k_r\rho_i^T < k_r\rho_{\theta i}^T$, both FLR effect and FOW effect should be considered. In addition, since strongly passing particles' condition is not negligible, I use $E \simeq \mu B_0(1+2\epsilon\kappa)$. So, flux surface averaged n_{nc} for trapped particles can be expressed as following with the approximation for Bessel function,

$$\begin{aligned} n_{nc,b} &= Z|e|\delta\phi\left(\frac{\epsilon T}{m^3}\right)^{1/2}\int_0^\infty\int_0^1\sqrt{8}\pi d\kappa dx\frac{\omega_{||}}{\omega_b} \\ &\times\ xJ_0^2(k_r\rho_i^T x)\left\{1-J_0^2(\alpha a_1(\kappa))\right\}\left(-\frac{\partial}{\partial x}\right)F(x) \\ &\simeq Z|e|\delta\phi\left(\frac{\epsilon T}{m^3}\right)^{1/2}\frac{4}{\pi k_r\rho_i^T} \\ &\times\ \left[\sqrt{8}F(0)+\frac{C_b}{\pi\sqrt{\epsilon}k_r\rho_{\theta i}^T}\int_0^\infty dx\frac{1}{x}\frac{\partial}{\partial x}F(x)\right] \end{aligned} \tag{64}$$

Similarly, I can get n_{nc} for passing particle as

$$\begin{aligned} n_{nc,t} &= Z|e|\delta\phi\left(\frac{\epsilon T}{m^3}\right)^{1/2}2\int_0^\infty\int_1^\infty\frac{\sqrt{8}\pi}{(1+2\epsilon\kappa)^{3/2}}d\kappa dx\frac{\omega_{||}}{\omega_t} \\ &\times\ xJ_0^2(\frac{k_r\rho_i^T x}{\sqrt{1+2\epsilon\kappa}})\left\{1-J_0^2(\alpha b_2(\kappa))\right\}\left(-\frac{\partial}{\partial x}\right)F(x) \\ &\simeq Z|e|\delta\phi\left(\frac{\epsilon T}{m^3}\right)^{1/2}\frac{4}{\pi k_r\rho_i^T} \\ &\times\ \left[\sqrt{8}(\frac{\pi^2}{\sqrt{32\epsilon}}-1)F(0)+\frac{C_t'}{\pi\sqrt{\epsilon}k_r\rho_{\theta i}^T}\int_0^\infty dx\frac{1}{x}\frac{\partial}{\partial x}F(x)\right], \end{aligned} \tag{65}$$

where

$$C_t' = \int_1^\infty d\kappa\frac{K(\kappa^{-1})}{\sqrt{\kappa(1+2\epsilon\kappa)}b_2(\kappa)} \tag{66}$$

Therefore, n_{nc} for Maxwellian distribution becomes

$$\frac{n_{nc,b}}{n_0} = \frac{4\sqrt{\epsilon}}{\pi^{5/2}k_r\rho_i^T}\left[1-\frac{C_b}{4\sqrt{\pi\epsilon}k_r\rho_{\theta i}^T}\right]\frac{Z|e|\delta\phi}{T} \tag{67}$$

$$\frac{n_{nc,t}}{n_0} = \frac{4\sqrt{\epsilon}}{\pi^{5/2}k_r\rho_i^T}\left[\left(\frac{\pi^2}{\sqrt{32\epsilon}}-1\right)-\frac{C_t'}{4\sqrt{\pi\epsilon}k_r\rho_{\theta i}^T}\right]\frac{Z|e|\delta\phi}{T} \tag{68}$$

Whereas, n_{nc} for slowing down distribution can be expressed as

$$\frac{n_{nc,b}}{n_0} = \frac{A_4}{3A_2^2}\frac{\sqrt{8\epsilon}}{\pi^2k_r\rho_c}\left[1-\frac{3C_b}{\sqrt{8\epsilon}\pi k_r\rho_{\theta c}}B_1\right]\frac{Z|e|\delta\phi}{T} \tag{69}$$

$$\frac{n_{nc,t}}{n_0} = \frac{A_4}{3A_2^2}\frac{\sqrt{8\epsilon}}{\pi^2k_r\rho_c}\left[\left(\frac{\pi^2}{\sqrt{32\epsilon}}-1\right)-\frac{3C_t'}{\sqrt{8\epsilon}\pi k_r\rho_{\theta c}}B_1\right]\frac{Z|e|\delta\phi}{T} \tag{70}$$

where

$$B_n = \int_0^{v_\alpha/v_c}\frac{x^n}{(1+x^3)^2}dx \tag{71}$$

IV.A.4.e. Connection formula for neoclassical polarization density

Then, I construct the connection formula which is valid for arbitrary wavelengths as I did for the classical polarization density. In this procedure, both trapped and passing particle contributions are included. As a result, the neoclassical polarizability is[53],

$$\chi_{nc,k} = \left\{\frac{1}{\chi_{nc}^{long}}+\frac{1}{1+(k_r\rho_i^T)^2}\frac{1}{\chi_{nc}^{med}}+\frac{(k_r\rho_i^T)^2}{1+(k_r\rho_i^T)^2}\frac{1}{\chi_{nc}^{short}}\right\}^{-1} \tag{72}$$

where χ_{nc}^{long}, χ_{nc}^{med}, and χ_{nc}^{short} are the neoclassical polarizabilities in the range of long, intermediate, and short wavelength respectively. χ_{nc} for F_M are given as

$$\chi_{nc}^{long} = 1.63\epsilon^{3/2}\left(k_r\rho_{\theta i}^T\right)^2, \tag{73}$$

$$\chi_{nc}^{med} = 1-\sqrt{\frac{2}{\pi^5}}\frac{(C_b+C_t)}{k_r\rho_{\theta i}^T}, \tag{74}$$

$$\text{and}\quad \chi_{nc}^{short} = \sqrt{\frac{1}{2\pi}}\frac{1}{k_r\rho_i^T}\left[1-\sqrt{\frac{2}{\pi^5}}\frac{C_b+C_t'}{k_r\rho_{\theta i}^T}\right] \tag{75}$$

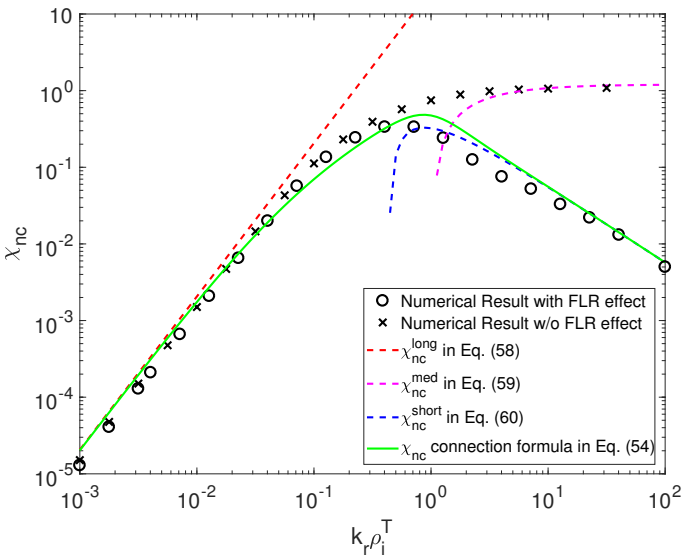

FIG. 17: Analytic and numerical results of χ_{nc} for F_{SD} in the wavelength range $10^{-3} \leq k_r\rho_i^T \leq 10^2$. Here, ρ_i^T is the Larmor radius of energetic particles.

Whereas, χ_{nc} for F_{SD} in each wavelength regime is

$$\chi_{nc}^{long} = 1.63\epsilon^{3/2}\left(k_r\rho_{\theta i}^T\right)^2, \tag{76}$$

$$\chi_{nc}^{med} = \frac{A_0 A_4}{3A_2^2}\left[1 - \frac{C_b + C_t}{\pi^2 A_0 k_r \rho_{\theta c}}\right], \tag{77}$$

$$\text{and} \quad \chi_{nc}^{short} = \frac{A_4}{6A_2^2}\frac{1}{k_r\rho_c}\left[1 - \frac{6(C_b + C_t')}{\pi^3 k_r \rho_{\theta c}}B_1\right] \tag{78}$$

χ_{nc} for F_{SD} depends on the electron temperature, since slowing down distribution is determined by collision between energetic ions and background particles. For instance, v_c in Eq. (23) depends on T_e.

Before I discuss behavior of the χ_{nc} in detail, I compare the numerical result for χ_{nc} with the analytic results in Fig. 17. Here, $T_e = 10keV$, $q = 2.0$, and $\epsilon = 0.1$. For numerical calculation, I use Eqs. (34) and

(35). Also, I plot another numerical calculation result without FLR effect by setting $J_0^2(k_r\rho_i^T x) \rightarrow 1$. Numerical result slightly overpredicts χ_{nc} in long wavelength regime since approximations of eikonal factors for bounce/transit motion used in Eqs. (51) and (52) do not fully include the second order term in $k_r\rho_\theta$. However the analytic result in Eq. (76) explains the overall trend in this regime well. Since the FLR effects are not considered when χ_{nc}^{med} is analytically calculated, Eq. (77) shows poor agreement with numerical result which includes FLR effect. Thus, I derive the χ_{nc}^{med} which includes FLR effect in the Appendix. Eq. (B8) yields a better agreement with the numerical result in the intermediate wavelength regime. χ_{nc}^{short} behaves similarly to the numerical result which includes FLR effect. It is noticeable that 1st term of R.H.S. of Eq. (78) is dominant for χ_{nc}^{short} at $k_r\rho_i^T > 1$ because of high aspect ratio limit. Therefore, it is the FLR effect, not the FOW effect which plays crucial role in determining behavior of χ_{nc}^{short}. Connection formula overestimates χ_{nc} in the intermediate wavelength regime including the $k_r\rho_i^T \sim 1$ range, because of FLR effect. Interestingly, the regime where connection formula overestimates the value is almost the same for χ_{cl} and χ_{nc}. I will examine this issue in terms of residual zonal flow level in the next section.

I plot χ_{nc} with $q = 2.0$ and $\epsilon = 0.1$ using numerical results for different temperature and distribution function in Fig. 18 a). Here, the black curve represents the χ_{nc} for both cases of thermal ions at $T_e = 10keV$ and $30keV$, because χ_{nc} for F_M is a function of $k_r\rho_i^T$. Unlike χ_{nc} for F_M, the maximum value of χ_{nc} ($Max(\chi_{nc})$) varies as a function of T_e for F_{SD}. In addition, $k_r\rho_{i,eff}$ for $Max(\chi_{nc})$ for F_{SD} becomes lower than that for F_M

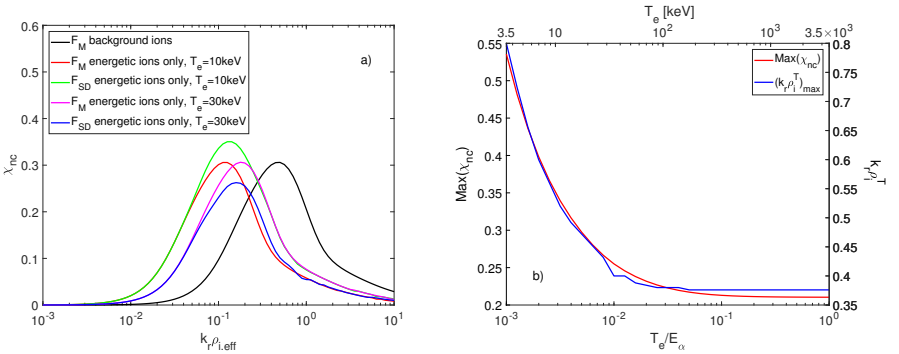

FIG. 18: a) Numerical results of χ_{nc} for different values of T_e and distribution functions. Here, $\rho_{i,eff}$ is the effective Larmor radius of background ions for corresponding T_e and $\bar{E}_M = \bar{E}_{SD}$ for energetic ions. The black curve represents χ_{nc} for both cases of thermal ions with $T_e = 10keV$ and with $30keV$. b) Maximum value of χ_{nc} and corresponding $k_r\rho_i^T$ for F_{SD}. Upper x-axis shows T_e when $E_\alpha = 3.5MeV$.

when $T_e = 30keV$.

To understand this trend in detail, Fig. 18 b) is plotted to show the maximum value of χ_{nc} and $(k_r\rho_i^T)_{max}$ for F_{SD} as a function of T_e/E_α. Here, $(k_r\rho_i^T)_{max}$ is defined by $\chi_{nc}((k_r\rho_i^T)_{max}) = Max(\chi_{nc})$. Maximum value of χ_{nc} decreases as T_e/E_α increases, and saturates to a certain level which is similar to the behavior of χ_{cl} for F_{SD}. From Eq. (B8), $\chi_{nc}^{med} \propto A_4/A_2$, which is proportional to the $\bar{E}_{SD}/T_c$. As T_e/E_α increases, T_c increases faster than $\bar{E}_{SD}$. This explains the reason why $Max(\chi_{nc})$ decreases. $(k_r\rho_i^T)_{max}$ also behaves like $Max(\chi_{nc})$. So, $Max(\chi_{nc})$ occurs at lower $k_r\rho_i^T$ for hotter background plasma. In addition, when $T_e/E_\alpha \gtrsim 4.0\times10^{-3}$ ($T_e \gtrsim 15keV$), χ_{nc} for F_{SD} takes a maximum value at lower $k_r\rho_i^T$ than that

for F_M.

IV.B. Residual Zonal Flow Level

IV.B.1. Physics of Residual Zonal Flow

In the previous sections, I have derived the analytic expressions of the classical and neoclassical polarization densities. Before I address the role of energetic ions on the residual zonal flow, I emphasize the role of the classical and neoclassical polarization densities on the residual zonal flow. Among the theories on residual zonal flow level, I take "the fixed steady source"[38] approach[51–53].

Since zonal flow is generated by turbulent Reynolds stress, the time scale of the initial generation ($t = 0$ in 1) is much longer than the ion gyration periods, but shorter than the bounce time, i.e., $\Omega_{ci}^{-1} << t < \omega_{bi}^{-1}$. So the zonal potential is shielded by the gyrating charged particles, which feel gyro-averaged electric potential and gyroangle dependent potential at the same time. Classified by the gyroangle dependency, the formal one corresponds to the perturbed gyrocenter density and the latter one corresponds to the classical polarization density (n_{cl}). But the non-adiabatic response cancels the perturbed gyrocenter density, and only n_{cl} remains and shielding the electric potential. As a result, perturbed density and zonal potential at $t = 0$ satisfy

$$\frac{n_{cl}}{n_0} = \chi_{cl} \frac{Z|e|\delta\phi(t=0)}{T} \tag{79}$$

Relaxation of the

Taking "the fixed steady source"[38] approach[51–53], the residual zonal flow level R_{ZF} can be expressed in terms of the classical polarization shielding quantified by the classical polarizability χ_{cl} due to finite ion Larmor radius(FLR) effects which occur at several ion gyration (short term) time scale and the neoclassical polarization shielding quantified by the neoclassical polarizability χ_{nc} due to finite ion orbit width(FOW) effects which occur at several ion bounce period (long term) time scale[1, 51].

$$R_{ZF} = \frac{\delta\phi(\infty)}{\delta\phi(0)} = \frac{\chi_{cl}}{\chi_{cl} + \chi_{nc}} \tag{80}$$

Since Rosenbluth and Hinton have considered the long wavelength regime ($k_r\rho_i < k_r\rho_{bi} \ll 1$) only and have not given detailed discussion in their letter[1], it is understandable that other approaches have also been taken for its extension to arbitrary wavelengths[54, 55, 66]. Refs. 54, 55, 66 showed that the final results for $\delta\phi(\infty)/\delta\phi(0)$ can depend on the choice of δf at $t = 0$. In particular, the short wavelength behavior of the residual zonal flow level becomes quite different for different choices of "$\delta f(0)$". Figs. 7, B1, and B2 of Ref. 54 and Figs. 2, 5, 6, and 13 of Ref. 55 exhibit the differences.

I note that, for instance, Ref. 54 has solved the lowest order linear gyrokinetic equation explicitly as an initial value problem for $\omega \ll \omega_{bi}$. Due to the frequency ordering and the reciprocal relation between t and ω (similar to the uncertainty principle in quantum mechanics) for this procedure, their lowest order gyrokinetic equation (essentially the bounce/transit-kinetic equation) can only resolve phenomena which occur with a coarse-grained time scale $\Delta t \gg \omega_{bi}^{-1}$. Therefore, it can provide a rigorous and accurate description[58] of the evolution of a system consisting of zonal

flows and trapped ion modes[79, 80]. On the other hand, the bounce-kinetic equation cannot describe the geodesic acoustic mode (GAM) which occurs with a characteristic time scale of $(v_{th,i}/R)^{-1} < \omega_{bi}^{-1}$. The GAM is not effective in regulating the core turbulence due to its relatively high frequency[26]. So it's unimportant compared to the zero-frequency residual zonal flows considered in this work and the previous publications on this issue. It is noteworthy that the analytic results from the lowest order gyrokinetics agree well with those from the gyrokinetic simulations with the same initial δf (but without the frequency ordering of $\omega \ll \omega_{bi}$), for a wide radial wavenumber region[54]. In addition, the initial value problem approach[1, 54, 55, 66] can reveal the detailed long term evolution of the zonal flows, and can be used for various applications for which more information than just $\delta\phi(\infty)/\delta\phi(0)$ is required for an assessment of particular effects. For instance, the effects of the resonant magnetic perturbation on the long term evolution of zonal flows have been evaluated using the initial value problem approach[63].

On the other hand, the fixed steady source approach that I have taken has its own attractiveness of a simple characterization of the residual zonal flows based on a physical picture of the polarization shielding[1, 38, 58]. Gyrokinetic simulation can also be set up for the fixed steady source approach[50, 54, 55], and a connection formula[53] based on Eq. (80) recovers the simulation results in Ref. 50 reasonably well for a wide range of radial wavenumber. In conclusion, I believe different results from two different approaches are not necessarily in conflict with one another.

I can express the residual zonal flow level in terms of classical and

neoclassical polarization density for multi-species ion plasmas,

$$
\begin{aligned}
R_{ZF} &= \frac{\sum_j n_{j,cl}}{\sum_j (n_{j,cl} + n_{j,nc})} \\
&= \frac{\frac{n_{0i}}{n_{0e}}\chi_{i,cl} + Z_\alpha^2 \tau_\alpha^{-1} \frac{n_{0\alpha}}{n_{0e}} \chi_{\alpha,cl}}{\frac{n_{0i}}{n_{0e}}(\chi_{i,cl} + \chi_{i,nc}) + Z_\alpha^2 \tau_\alpha^{-1} \frac{n_{0\alpha}}{n_{0e}} (\chi_{\alpha,cl} + \chi_{\alpha,nc})}
\end{aligned}
\tag{81}
$$

Here, Z_α is the charge of α particle and $\tau_\alpha = T_{eff}/T_i$. One should be careful about the fact that n_{cl} and n_{nc} are weighted by different temperatures so that I cannot simply add up dimensionless polarizabilities in numerator and denominator. Thus, not only the χ_{cl} and χ_{nc}, but also the $Z_\alpha^2 n_\alpha / n_0$ and temperature ratio (τ_α) affect the residual zonal flow level. This observation is crucial when impurity effects on the residual zonal flow are estimated as emphasized in Ref. 62. Ref. 62 reports that 10% concentration of moderately high temperature Helium (with $T_{eff}/T_{e,i} = 10$) impurities with Maxwellian distribution can lead to a considerable enhancement of R_{ZF} in the intermediate wavelength range of $k_r \rho_{i,eff} \sim 0.5$. My results for fusion product α-particles with high equivalent temperature ratio ($\tau_\alpha = T_{eff}/T_i \sim 30$ for $T_e = 30keV$) exhibit a similar trend for both slowing down and Maxwellian α-particle distribution functions.

I plot the residual zonal flow level (R_{ZF}) for F_{SD} with $q = 2.0$, $\epsilon = 0.1$, and $T_e = 10keV$ for analytic and numerical results in Fig. 19. Numerical result overestimates residual zonal flow a bit in long wavelength regime because of an approximate treatment of an eikonal factor in χ_{nc}, as mentioned in previous section. Near $k_r \rho_i^T \sim 1$, analytic result overestimates χ_{cl} and χ_{nc}, and slightly overestimates residual zonal flow. So, I construct the following connection formula for χ_{nc} to get more accurate residual

zonal flow level.

$$\chi_{nc} = \left\{ \frac{1}{1+(k_r\rho_{\theta i}^T)^2}\frac{1}{\chi_{nc,A}} + \frac{(k_r\rho_{\theta i}^T)^2}{1+(k_r\rho_{\theta i}^T)^2}\frac{1}{\chi_{nc,N}} \right\}^{-1} \tag{82}$$

Here, $\chi_{nc,A}$ is the analytic result of χ_{nc} and $\chi_{nc,N}$ is the numerical result of χ_{nc}. The blue dashed-curve from the numerical result for χ_{cl} and Eq. (82) for χ_{nc} accurately represents the behavior of R_{ZF} throughout all wavelength regime. Thus, I use Eq. (82) for χ_{nc} to analyze the R_{ZF}.

Figs. 20 a) and b) show the residual zonal flow for different T_e and distribution functions. For residual zonal flow level for F_M, τ_α only affects the $k_r\rho_{i,eff}$ range where a transition from long wavelength regime to short wavelength regime occurs. On the other hand, the residual zonal flow level for F_{SD} in the transition regime depends on T_e and becomes higher

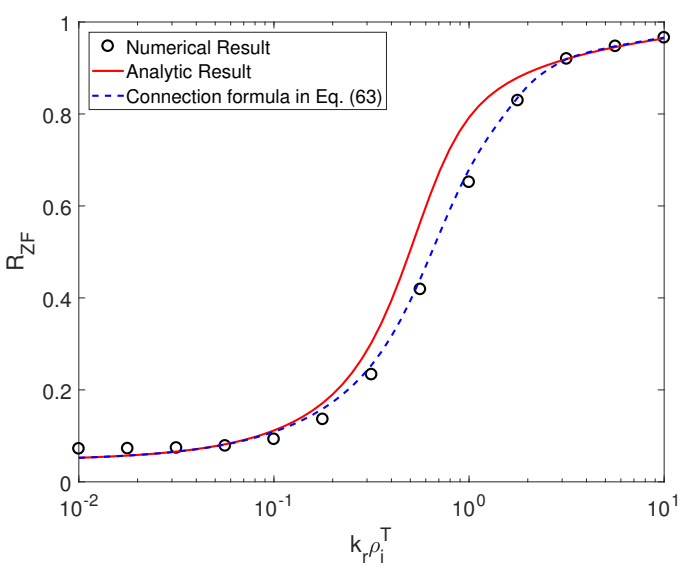

FIG. 19: Analytic and numerical results of R_{ZF} for F_{SD} in the wavelength range, $10^{-2} \leq k_r\rho_i^T \leq 10$. Here, $q = 2.0$, $\epsilon = 0.1$, and $T_e = 10keV$.

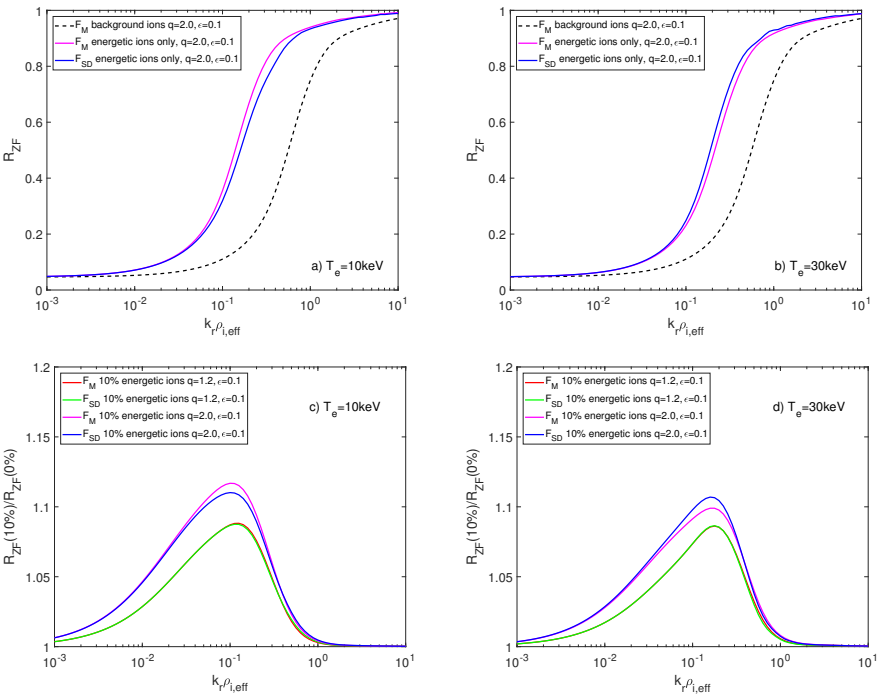

FIG. 20: Numerical results of R_{ZF} for different distribution functions in the wavelength range, $10^{-2} \leq k_r\rho_{i,eff} \leq 10$ for D-T plasma with a) $T_e = 10keV$ and b) $T_e = 30keV$. Enhancement of residual zonal flow level due to the presence of 10% concentration of energetic ions for D-T plasma with c) $T_e = 10keV$ and d) $T_e = 30keV$.

(lower) than that for F_M for $T_e = 30keV$ $(10keV)$. This is because of the transition characteristics of χ_{nc} for F_{SD}. From Fig. 18 b), $Max(\chi_{nc})$ occurs at lower $k_r\rho_i^T$ for higher T_e/E_α. Therefore, transition of R_{ZF} for F_{SD} to the shorter wavelength regime occurs at lower $k_r\rho_i^T$ comparing to that for F_M for hotter background plasma. Unless T_e is too low compared to E_α (i.e. if $T_e/E_\alpha \gtrsim 5.0\times10^{-3}$, $T_e \gtrsim 20keV$ for $E_\alpha = 3.5MeV$), energetic

ions with F_{SD} can increase the residual zonal flow more than those with F_M. Enhancement of residual zonal flow level due to 10% concentration of energetic ions is plotted in Figs. 20 c) and d). As shown in Figs. 20 a) and b), energetic ions with F_{SD} enhance R_{ZF} more than those with F_M at $T_e = 30keV$. Enhancement at $k_r\rho_{i,eff} \sim 10^{-1}$ is greater for higher q, since the residual zonal flow level of background plasmas in the long wavelength is relatively lower. Thus, for the cases with higher electron temperature target plasmas in ITER with fusion products, the energetic ions with F_{SD} should exhibit more enhancement of the residual zonal flow level.

Finally, for zonal flows with even shorter wavelengths relevant to ETG-turbulence, the electron dynamics should be included. Useful results on this from an initial value problem approach can be found in Figs. 4, 5, and 8 in Ref. 54.

IV.C. Discussions

Residual zonal flow level for non-Maxwellian distribution, especially the slowing down distribution, has been systematically calculated in arbitrary wavelength regime in this work. The classical and neoclassical polarization density are derived from the general expressions which are obtained from the modern gyrokinetic approach via pull-back transform from gyro/bounce-center Lagrangian to phase-space Lagrangian using Lie-transform perturbation method[53, 72, 77]. To elucidate the FOW effect more accurately, I use explicit compact expressions for orbit-averaged eikonal factor $\left\langle e^{i\Delta\zeta}\right\rangle_{b,t}$ which consider full finite-orbit effects with arbitrary pitch angle parameter values[72]. χ_{cl} and χ_{nc} for slowing down distribu-

tion function are analytically derived in the whole wavelength regime by systematically considering the FLR effect and FOW effect in each wavelength limit and by constructing a connection formula. As a result, my analytic result describes the residual zonal flow level for slowing down distribution function pretty well.

Analytic expressions for χ_{cl} and χ_{nc} in the long wavelength limit are found to be the same for any well-defined distribution function which is isotropic in velocity space. As a consequence, residual zonal flow level in the long wavelength regime is the same as the Rosenbluth-Hinton expression for any isotropic distribution function in the high aspect ratio limit[1]. Asymptotic level of χ_{cl}^{short} and maximum value of χ_{nc} for F_{SD} decrease as T_e/E_α increases. As a result, the contribution of energetic particles on χ_{cl} and χ_{nc} becomes greater as energy of energetic particles normalized to the electron temperature increases. Maximum value of χ_{nc} also occurs at lower $k_r\rho_i^T$ for higher T_e/E_α.

My analytic results of residual zonal flow for slowing down distribution show good agreement with the numerical results and provide an understanding of its behavior. For a plasma with $T_e = 10keV$, $n_\alpha/n_e = 0.1$, $q = 2.0$, and $\epsilon = 0.1$, approximately 12% enhancement of residual zonal flow level at $k_r\rho_{i,eff} \sim 10^{-1}$ regime is expected. When $T_e/E_\alpha \gtrsim 5.0 \times 10^{-3}$ or $T_e \gtrsim 20keV$, my results predict that energetic alpha particles with slowing down distribution enhance the residual zonal flow level more than those with Maxwellian distribution.

Recently, electromagnetic gyrokinetic simulation using parameters from JET experiment emphasized the importance of coupling of fast ions

and electromagnetic effects on the stabilization of ITG turbulence[81, 82]. Based on Eq. (81) of this paper, approximately 5% enhancement of residual zonal flow in the range of $k_r\rho_{i,eff} \sim 0.1$ is expected for JET-like plasmas[83] due to the fast ion effect. This favorable trend from my electrostatic calculation is encouraging, but does not seem significant enough to fully explain the results in Refs. 81, 82. Ref. 84 on the other hand, indicates that turbulence and zonal flows interact for a longer time as β increases. So electromagnetic effect could make the stabilizing influence of zonal flows more efficient. Therefore, an extension of my work including the electromagnetic effects can bring a deeper insight on the aforementioned results[81, 82] for JET-like plasmas and projection to ITER. For instance, combined effects of fast ions and finite β can boost zonal flows even further.

V. CONCLUSION

In this thesis, I addressed my research on $E \times B$ flow through theory, simulation, and experiment. I analyzed the in-out asymmetry of $E \times B$ flow shear via analytic derivation of its R dependency, and observation in simulation using δf gyrokinetic code gKPSP. I figured out that $E \times B$ shearing rate ω_E is proportional to R^1 in the usual concentric circular flux surface structure in gyrokinetic simulations. From the gyrokinetic simulations, I found that turbulence correlation time is also longer at the low field side (LFS), and thus $\tau_c \omega_E$ is considerably higher at the LFS than that at the high field side (HFS). As a result, the reduction of the fluctuations such as $\delta\phi$ and their radial correlation length is stronger at the LFS as $\tau_c \omega_E$ becomes higher, which weakens the poloidal dependency of the fluctuations and its radial correlation length.

To extend this work, I estimated the in-out asymmetry of ω_E in the KSTAR experiments using ECEI and CES data. At first, I compared the group velocity v_{gp} calculated from the ECEI data to the $E \times B$ velocity $v_{E\times B}$ calculated by the radial force balance equation. Though v_{gp} was slower than $v_{E\times B}$ and their estimations on the location of the transport barrier differed, their shear was similar. Thus, I considered the shear of v_{gp} as ω_E to analyze the in-out asymmetry of ω_E and its effect on the fluctuations. In-out asymmetry of $\omega_E (\propto R^{2.1})$ was calculated to be stronger than that in the gyrokinetic simulation in the concentric circular flux surface ($\propto R^1$). Comparison between τ_c and ω_E corresponded to the formation of the edge transport barrier. However, a more detailed analysis of the fluctuation was required because of the ELM and MHD instabilities.

As a theoretical analysis, I studied the role of non-Maxwellian energetic ions on the residual zonal flow. To investigate the effects of energetic ions, I used slowing-down distribution F_{SD}, which provides a precise description of energetic ions. Based on the modern gyrokinetic/bouncekinetic formalism, classical polarization density n_{cl} and neoclassical polarization density n_{nc} for F_{SD} were derived in the all wavelength range. I figured out that n_{cl} and n_{nc} are the same for any isotropic distribution in the long-wavelength limit, and thus residual zonal flow R_{ZF} in the long-wavelength regime is the same as Rosenbluth-Hinton residual zonal flow level for arbitrary isotropic distributions. Energetic ions enhance the R_{ZF} mainly at the intermediate wavelength regime $k_r\rho_i < 1 < k_r\rho_{ib}$. And F_{SD} enhances the R_{ZF} more than Maxwellian F_M if background electron temperature $T_e \gtrsim 20keV$.

As future work, I complement the research on in-out asymmetry of the ω_E in the KSTAR plasma using the ECEI data. Present research in Sec. III has the following shortcomings. The plasma moved down during it was measured by CES. Although the current estimation on v_{gp} based on ECEI data shows good agreement with the $v_{E\times B}$ deduced from the radial profiles of T_i and v_T measured by CES, it still has a problem on its reliability. Besides, because of the ELM and MHD instabilities, it is difficult to analyze the reduction of the fluctuations by $E \times B$ flow shear. To complement those shortcomings, additional experimental data measured by CES and ECEI at the same time is needed. Especially, the reason why the estimation of the transport barrier is different between the two measurements should be figured out to estimate the ω_E more clearly.

Also, the present numerical scheme to estimate the v_{gp}, RANSAC, should be changed to the other numerical scheme. Since there is too much 'outlier' in ECEI data, RANSAC gives the results with too high uncertainty. And the comparison with the gyrokinetic simulation on the same flux surface can enhance the understanding of the in-out asymmetry of the ω_E and fluctuations.

I finish the conclusion by addressing the possible applications of my research in the future. The research on the in-out asymmetry of ω_E via analytic theory, simulation, and experiment can be used to enhance the confinement by constructing the magnetic flux surface. The numerical scheme to calculate the $v_{E\times B}$ using ECEI data can provide the ω_E even without the experiments without the NBI modulation since CES is applicable only when NB is injected. My analytic derivation of the residual zonal flow for non-Maxwellian distribution can be applied to test the gyrokinetic simulation with non-Maxwellian distributions. One of the initial benchmark simulations for gyrokinetic code is the residual zonal flow test in the long-wavelength limit. When they introduce the non-Maxwellian distribution like F_{SD}, my derivation can be used as the reference for the residual zonal flow test. In addition, the research on the role of energetic ions on residual zonal flow introduces the other possible stabilization effects of the energetic ions. I wish my research contributes to the success of the ITER and commercial nuclear fusion plant in the future.

Appendix A. (for Sec. II)

To clarify the effect of collisionality on the self-regulation dynamics between turbulence and zonal flow, we plot zonal flow intensity as a function of turbulence intensity for different collisionalities in Fig. 21. The self-regulation dynamics exhibit limit cycle oscillations. Especially, it is visible that as collisionality increases, the mean value and the oscillation amplitude of the zonal flow intensity are reduced. So, the overall zonal flow level decreases with collisionality, as anticipated from the collisional damping of zonal flow. However in short time intervals, the inversely proportional relation between zonal flow level and collisionality is not apparent because of the overlap of the limit cycle orbits.

The observed collisionality dependence of the self-regulation dynamics can be understood from a simple predator-prey (or Lotka-Volterra) model:[22]

$$\frac{\partial}{\partial t}N = \gamma N - \alpha U N, \tag{83}$$

$$\frac{\partial}{\partial t}U = \alpha N U - \gamma_d U. \tag{84}$$

where $N = \phi^2$ and $U = V_E^2$ are turbulence intensity and zonal flow energy, respectively. Here, γ, γ_d, and α are the linear growth of turbulence, the collisional damping of zonal flow, and the coefficient of nonlinear energy transfer between turbulence and zonal flow, respectively. Nonlinear damping terms such as $\Delta\omega N^2$ and $\gamma_{NL}U^2$ are neglected for simplicity. It is well-known that the predator-prey equations have limit cycle solutions due to the existence of the unstable fixed point $(N_0, U_0) = (\gamma_d/\alpha, \gamma/\alpha)$,

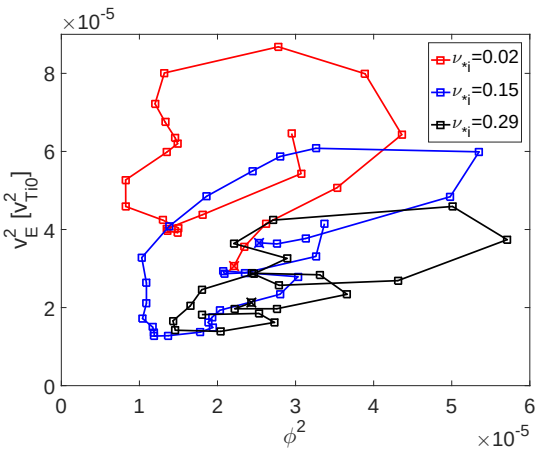

FIG. 21: Limit Cycle Oscillations for different values of collisionality. Boxes in the same color lines evolve in time along a line starting from the box with 'X' mark. Time interval for each simulation result is chosen differently in order to show one complete cycle. (from $t/(R_0/v_{Ti0}) = 250$ to 360 for $\nu_{*i} = 0.02$, from $t/(R_0/v_{Ti0}) = 250$ to 400 for $\nu_{*i} = 0.15$, and from $t/(R_0/v_{Ti0}) = 200$ to 310 for $\nu_{*i} = 0.29$)

which corresponds the center of the limit cycle oscillations. And the eigenvalue and eigenmode of the oscillation are given by $\lambda = \pm i\sqrt{\gamma\gamma_d}$ and $\tilde{U} = \mp i\sqrt{\gamma/\gamma_d}\tilde{N}$, respectively. Since $\gamma_d \propto \nu_{ii}$, the mean value ratio U_0/N_0 and the oscillation amplitude ratio of zonal flow to turbulence $|\tilde{U}/\tilde{N}|$ decrease as collisionality increases. Thus, the collisionality dependence of the limit cycle oscillations in Fig. 21 is captured by the simple predator-prey in a qualitative sense. Another gyrokinetic simulation study on collisionality dependence of predator-prey dynamics has been performed in magnetic shearless plasma in Ref. 29.

Appendix B. Refinement of neoclassical polarization formula including the finite Larmor radius effect (for Sec.IV)

In Sec. IV. A. 4, we derived χ_{nc}^{med} in Eqs. (62) and (63). However, since the FLR effect is ignored in Eq. (55), χ_{nc}^{med} shows poor agreement with numerical result as shown in Fig. 17. It results in the 60% overestimation of χ_{nc} in the intermediate wavelength regime. So, in this appendix, we derive the χ_{nc}^{med} in the intermediate wavelength regime including the FLR effect. For the intermediate wavelength regime, χ_{nc} is calculated from

$$\begin{aligned} n_{nc,b} &= Z|e|\delta\phi\left(\frac{\epsilon T}{m^3}\right)^{1/2}\int_0^\infty\int_0^1\sqrt{8}\pi d\kappa dx\frac{\omega_{||}}{\omega_b}x \\ &\times\ J_0^2(k_r\rho_i^T x)\left\{1-J_0^2(\alpha a_1(\kappa))\right\}\left(-\frac{\partial}{\partial x}\right)F(x) \\ &\simeq Z|e|\delta\phi\left(\frac{\epsilon T}{m^3}\right)^{1/2}\int_0^\infty\int_0^1\sqrt{8}\pi d\kappa dx\frac{2K(\kappa)}{\pi}x \\ &\times\ J_0^2(k_r\rho_i^T x)\left\{1-\frac{1}{\sqrt{2\epsilon}\pi a_1 k_r\rho_{\theta i}^T x}\right\}\left(-\frac{\partial}{\partial x}\right)F(x) \end{aligned} \tag{B1}$$

$$\begin{aligned} n_{nc,t} &= Z|e|\delta\phi\left(\frac{\epsilon T}{m^3}\right)^{1/2}2\int_0^\infty\int_1^\infty\sqrt{8}\pi d\kappa dx\frac{\omega_{||}}{\omega_t}x \\ &\times\ J_0^2(k_r\rho_i^T x)\left\{1-J_0^2(\alpha b_2(\kappa))\right\}\left(-\frac{\partial}{\partial x}\right)F(x) \\ &\simeq Z|e|\delta\phi\left(\frac{\epsilon T}{m^3}\right)\int_0^\infty\int_1^\infty\sqrt{8}\pi d\kappa dx\frac{2K(\kappa^{-1})}{\pi\sqrt{\kappa}}x \\ &\times\ J_0^2(k_r\rho_i^T x)\left\{1-\frac{(1+2\epsilon\kappa)^{1/2}}{\sqrt{2\epsilon}\pi b_2 k_r\rho_{\theta i}^T x}\right\}\left(-\frac{\partial}{\partial x}\right)F(x) \end{aligned} \tag{B2}$$

For Maxwellian distribution function, we can directly calculate Eqs. (B1) and (B2) ignoring the effects from the strongly passing particles,

$$\begin{aligned}
\frac{n_{nc,b}}{n_0} &= \frac{Z|e|\delta\phi}{T}\left(\frac{2\epsilon}{\pi^3}\right)^{1/2} \\
&\times \left[2\sqrt{\pi}\,{}_2F_2\left(\left\{\frac{1}{2},\frac{3}{2}\right\},\{1,1\},-2(k_r\rho_i^T)^2\right)\right. \\
&- \left.\frac{C_b}{\pi\sqrt{\epsilon}k_r\rho_{\theta i}^T}\Gamma_0((k_r\rho_i^T)^2)\right]
\end{aligned} \tag{B3}$$

$$\begin{aligned}
\frac{n_{nc,t}}{n_0} &= \frac{Z|e|\delta\phi}{T}\left(\frac{2\epsilon}{\pi^3}\right)^{1/2} \\
&\times \left[2\sqrt{\pi}\left(\frac{\pi}{\sqrt{8\epsilon}}-1\right)\,{}_2F_2\left(\left\{\frac{1}{2},\frac{3}{2}\right\},\{1,1\},-2(k_r\rho_i^T)^2\right)\right. \\
&- \left.\frac{C_t}{\pi\sqrt{\epsilon}k_r\rho_{\theta i}^T}\Gamma_0((k_r\rho_i^T)^2)\right]
\end{aligned} \tag{B4}$$

$$\begin{aligned}
\chi_{nc} &= {}_2F_2\left(\left\{\frac{1}{2},\frac{3}{2}\right\},\{1,1\},-2(k_r\rho_i^T)^2\right) \\
&- \sqrt{\frac{2}{\pi^5}}\frac{C_b+C_t}{k_r\rho_{\theta i}^T}\Gamma_0((k_r\rho_i^T)^2).
\end{aligned} \tag{B5}$$

This covers both intermediate and short wavelength regime. Here, ${}_2F_2$ is the hypergeometric function and $\Gamma_0(x) = e^{-x}I_0(x)$. Comparison between numerical results from Eqs. (53) and (54), and analytic result from Eq. (B6) is plotted in Fig. 22 a). Except for the range $10^{-1} < k_r\rho_i^T < 5\times 10^{-1}$, Eq. (B6) gives more accurate χ_{nc} in the shorter wavelength regime compared to the Eqs. (75) and (76).

For F_{SD}, we use the approximation that $J_0^2(x) \simeq 1 - x^2/2$ for the term related to FLR effect. Then, Eqs. (B1) and (B2) become

$$\begin{aligned}
n_{nc,b} &= Z|e|\delta\phi\left(\frac{\epsilon T}{m^3}\right)^{1/2} 4\left[-\frac{C_b}{\pi\sqrt{\epsilon}k_r\rho_{\theta i}^T}F(0)\right. \\
&+ \left.\int_0^\infty dx F(x)\left\{\sqrt{8}+\frac{\sqrt{\epsilon}C_b}{\pi q}k_r\rho_i^T x - 3\sqrt{2}(k_r\rho_i^T)^2x^2\right\}\right]
\end{aligned} \tag{B6}$$

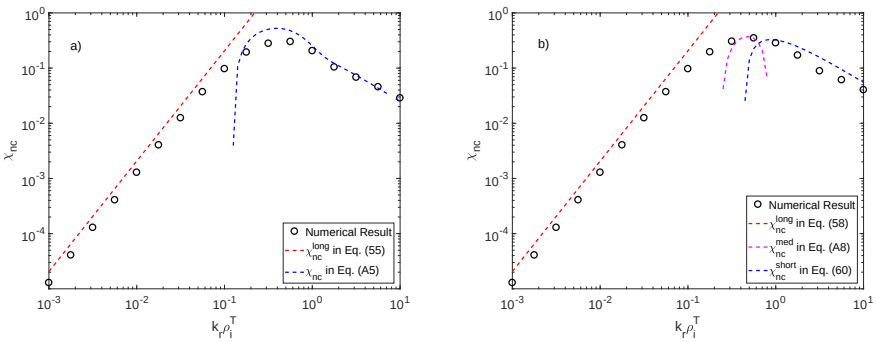

FIG. 22: Analytic and numerical results of χ_{nc} for a) F_M and b) F_{SD} in the wavelength range $10^{-2} \leq k_r\rho_i^T \leq 10$. Here, analytic results which cover the intermediate wavelength regime are calculated from Eqs. (B6) and (B8).

$$
\begin{aligned}
n_{nc,t} \;=\; & Z|e|\delta\phi\left(\frac{\epsilon T}{m^3}\right)^{1/2} 4\Bigg[-\frac{C_t}{\pi\sqrt{\epsilon}k_r\rho_{\theta i}^T}F(0) \\
& + \int_0^\infty dx F(x)\Bigg\{\sqrt{8}\left(\frac{\pi}{\sqrt{8\epsilon}}-1\right)+\frac{\sqrt{\epsilon}C_t}{\pi q}k_r\rho_i^T x \\
& - 3\sqrt{2}\left(\frac{\pi}{\sqrt{8\epsilon}}-1\right)(k_r\rho_i^T)^2x^2\Bigg\}\Bigg]
\end{aligned}
\tag{B7}
$$

For slowing down distribution function, χ_{nc}^{med} is

$$
\chi_{nc}^{med} \;=\; \frac{A_4}{3A_2}\left[\frac{A_0}{A_2}-\frac{3}{2}(k_r\rho_c)^2-\frac{C_b+C_t}{\pi^2A_2k_r\rho_{\theta c}}\left\{1-A_1(k_r\rho_c)^2\right\}\right] \tag{B8}
$$

Compared to Eq. (77), Eq. (B8) contains two additional terms (2nd and 4th terms in R.H.S) which are related to the FLR effect. Fig. 22 b) shows that Eq. (B8) has a better agreement with numerical result. However, Eqs (B6) and (B8) are difficult to use for constructing a connection formula since their Laurent series is not applicable to Eq. (73). In conclusion, the connection formula (Eq. (73)) and its elements (Eqs. (74-79)) in the

main text can lead to an overestimation of χ_{nc} (with a maximum of 60% at $k_r\rho_i^T \simeq 0.5$), as shown in Fig. 17. Nevertheless, this is not large enough to change any of our main conclusions in this paper.

References

[1] M. Rosenbluth and F. Hinton, *Phys. Rev. Lett.*, **80**, 724 (1998)

[2] H. Biglari, P.W. Terry, and P.H. Diamond, *Phys. Plasmas* **2**, 1 (1990)

[3] T.S. Hahm and K.H. Burrell, *Phys. Plasmas* **2**, 1648 (1995)

[4] W. Horton, Rev. Mod. Phys **71**, 735 (1999)

[5] X. Garbet, Y. Idomura, L. Villard, and T.H. Watanabe, Nucl. Fusion **50**, 043002 (2010)

[6] A. Fujisawa, A. Ouroua, J.W. Heard, T.P. Crowley, P.M. Schoch, K.A. Connor, R.L. Hickok, and A.J. Wootton, Nucl. Fusion **36**, 375 (1996)

[7] C. Watts, R.F. Gandy, and G. Cima, Phys. Rev. Lett. **76**, 2274 (1996)

[8] D.R. Demers, P.M. Schoch, T.P. Crowley, K.A. Connor, and A. Ouroua, Phys. Plasmas **8**, 1278 (2001)

[9] V.A. Vershkov, V.F.Andreev, A.A. Borschegovskiy, V.V. Chistyakov, M.M. Dremin, L.G. Eliseev, E.P. Gorbunov, S.A. Grashin, A.V. Khmara, A.Ya. Kislov *et al.*, Nucl. Fusion **51**, 094019 (2011)

[10] R. Sabot, F. Clairet, G.D. Conway, L. Cupido, X. Garbet, G. Falchetto, T. Gerbaud, S. Hacquin, P. Hennequin, S. Heuraux *et al.*, Plasma Phys. Control. Fusion **48**, B421 (2006)

[11] B. Lloyd, J-W. Ahn, R.J. Akers, L.C. Appel, D. Applegate, K.B. Axon, Y. Baranov, C. Brickley, C. Bunting, R.J. Buttery *et al.*, Plasma Phys. Control. Fusion **46**, B477 (2004)

[12] M. Ono, M.G. Bell, R.E. Bell, T. Bigelow, M. Bitter, W. Blanchard, J. Boedo, C. Bourdelle, C. Bush, W. Choe *et al.*, Plasma Phys. Control.

Fusion **45**, A335 (2003)

[13] T.L. Rhodes, R.J. Taylor, E.J. Doyle, Jr. N.C. Luhmann, and W.A. Peebles, Nucl. Fusion **33**, 1787 (1993)

[14] C.L. Rettig, K.H. Burrell, B.W. Stallard, G.R. McKee, G.M. Staebler, T.L. Rhodes, C.M. Greenfield, and W.A. Peebles, Phys. Plasmas **5**, 1727 (1998)

[15] Z. Lin, T.S. Hahm, W.W. Lee, W.M. Tang, and R.B. White, Science **281**, 1835 (1998)

[16] J.M. Kwon, S. Yi, T. Rhee, P.H. Diamond, K. Miki, T.S. Hahm, J.Y. Kim, Ö.D. Gürcan, and C. McDevitt, Nucl. Fusion **52**, 013004 (2012)

[17] T.S. Hahm, Phys. Fluids **31**, 2670 (1988)

[18] Z. Lin, W.M. Tang, and W.W. Lee, Phys. Plasmas **2**, 2975 (1995)

[19] W.X. Wang, N. Nakajima, M. Okamoto, and S. Murakami, Plasma Phys. Control. Fusion **41**, 1091 (1999)

[20] B.F. McMillan, S. Jolliet, T. M. Tran, L. Villard, A. Bottino, and P. Angelino, Phys. Plasmas **15**, 052308 (2008)

[21] Z. Lin, T.S. Hahm, W.W. Lee, W.M. Tang, and P.H. Diamond, Phys. Rev. Lett. **83**, 3645 (1999)

[22] P.H. Diamond, S-I. Itoh, K. Itoh, and T.S. Hahm, Plasma Phys. Control. Fusion **47**, R35 (2005)

[23] M.A. Malkov, P.H. Diamond, and M.N. Rosenbluth, Phys. Plasmas **8**, 5073 (2001)

[24] Y.Z. Zhang and S. M. Mahajan, Phys. Fluids B **4**, 1385 (1992)

[25] T.S. Hahm, Phys. Plasmas **1**, 2940 (1994)

[26] T.S. Hahm, M.A. Beer, Z. Lin, G.W. Hammett, W.W. Lee, and W.M.

Tang, Phys. Plasmas **6**, 922 (1999)

[27] T.S. Hahm, Plasma Phys. Control. Fusion **44**, A87 (2002)

[28] P.H. Diamond and Y.-B Kim, Phys. Fluids B **3**, 1626 (1991)

[29] S. Kobayashi, Ö.D. Gürcan, and P.H. Diamond, Phys. Plasmas **22**, 090702 (2015)

[30] R.C. Isler Plasma Phys. Control. Fusion **36**, 171 (1994)

[31] G.S. Yun et al., Rev. Sci. Instrum **85**, 11D820 (2014)

[32] M.J. Choi arXiv:1907.09184v3

[33] K.L. Wong et al., Phys. Lett. A. **236**, 339 (1997)

[34] M.A. Fischler and R.C. Bolles Comm. ACM **24**, 381 (1981)

[35] Y.W. Cho et al., Phys. Plasmas **23**, 102312 (2016)

[36] P.H. Diamond *et al* 1998 *17th IAEA Fusion Energy Conference* 1421

[37] L. Chen, R.B. White, and F. Zonca Phys. Rev. Lett. **92**, 075004 (2004)

[38] L. Wang and T.S. Hahm Phys. Plasma **16**, 082302 (2009)

[39] Z.B. Guo and T.S. Hahm Nucl. Fusion **56**, 066014 (2016)

[40] F.L. Hinton and R.H. Rosenbluth Plasma Phys. Control. Fusion **41**, A653 (1999)

[41] K. Itoh *et al* Phys. Plasmas **13**, 055502 (2006)

[42] D.K. Gupta *et al* Phys. Rev. Lett. **97**, 125002 (2006)

[43] A. Fujisawa*et al* Phys. Rev. Lett. **93**, 165002 (2004)

[44] T.S. Hahm *et al* Plasma Phys. Control. Fusion **42**, A205 (2000)

[45] C. Hidalgo*et al* Phys. Rev. Lett. **83**, 2203 (1999)

[46] Y.H. Xu *et al* Phys. Rev. Lett. **84**, 3867 (2000)

[47] G.S. Xu *et al* Phys. Rev. Lett. **91**, 125001 (2003)

[48] K.J. Zhao *et al* Phys. Rev. Lett. **96**, 255004 (2006)

[49] T. Happel *et al* Phys. Plasmas **18**, 102302 (2011)

[50] F. Jenko *et al* Phys. Plasmas **7**, 1904 (2000)

[51] Y. Xiao and P.J. Catto Phys. Plasmas **13**, 102311 (2006)

[52] E.J. Kim, C. Holland, and P.H. Diamond Phys. Rev. Lett. **91**, 075003 (2003)

[53] L. Wang and T.S. Hahm Phys. Plasmas **16**, 062309 (2009)

[54] P. Monreal *et al* Plasma Phys. Control. Fusion **58**, 045018 (2016)

[55] O. Yamagishi Plasma Phys. Control. Fusion **60**, 045009 (2018)

[56] D.H.E. Dubin *et al* Phys. Fluids **26**, 3524 (1983)

[57] T.S. Hahm Phys. Fluids **31**, 2670 (1988)

[58] B. Fong and T.S. Hahm Phys. Plasmas **6**, 188 (1999)

[59] T.S. Hahm *et al* Nucl. Fusion **53**, 072002 (2013)

[60] A. Bustos *et al* Phys. Plasmas **22**, 012305 (2015)

[61] J. Garcia *et al* Nucl. Fusion **57**, 014007 (2017)

[62] W.X. Guo, L. Wang, and G. Zhuang Nucl. Fusion **57**, 056012 (2017)

[63] G.J. Choi and T.S. Hahm Nucl. Fusion **58**, 026001 (2018)

[64] H. Sugama and T.-H. Watanabe Phys. Rev. Lett. **94**, 115001 (2005)

[65] H. Sugama and T.-H. Watanabe Phys. Plasmas **13**, 012501 (2006)

[66] P. Yamagishi and H. Sugama Phys. Plasmas **19**, 092504 (2012)

[67] Lee K.P. and Hahm T.S. 2017 Gyro-kinetic Study of Rosenbluth-Hinton Flow for Fusion Reactor Plasmas *M&C Conference (Jeju, April 2017)* P381S11-01

[68] M.N. Rosenbluth and F.L. Hinton Nucl. Fusion **36**, 55 (1996)

[69] P.W. Terry, M.J. Pueschel, D. Carmody, and W.M. Nevins Phys. Plasmas **20**, 112502 (2013)

[70] ITER Physics Basis Expert Group on Confinement and Transport and Confinement Modelling and Database, ITER Physics Basis Editor 1999 *Nucl. Fusion* **39** 2175

[71] S.H. Kim *et al* Nucl. Fusion **56**, 126002 (2016)

[72] F.-X. Duthoit, A.J. Brizard, and T.S. Hahm Phys. Plasmas **21**, 122510 (2014)

[73] J.D. Gaffey, Jr J. Plasma Physics **16**, 149 (1976)

[74] W.W. Lee Phys. Fluids **26**, 556 (1983)

[75] E.A. Frieman and L. Chen Phys. Fluids **25**, 502 (1982)

[76] A.J. Brizard and T.S. Hahm Rev. Mod. Phys. **79**, 421 (2007)

[77] F.-X. Duthoit, T.S. Hahm, and L. Wang Phys. Plasmas **21**, 122510 (2014)

[78] M. Abramowitz and I.A. Stegun Handbook of mathematical functions (New York: Dover Publications)

[79] B.B. Kadomtsev and O.P. Pogutse Nucl. Fusion **11**, 67 (1971)

[80] T.S. Hahm and W.M. Tang Phys. Plasmas **3**, 242 (1996)

[81] J. Citrin *et al.* Phys. Rev. Lett. **111**, 155001 (2013)

[82] J. Garcia *et al.* Nucl. Fusion **55**, 053007 (2015)

[83] J. Hobirk *et al.* Plasma Phys. Control. Fusion **54**, 095001 (2012)

[84] G.G. Whelan and M.J. Pueschel Phys. Rev. Lett. **120**, 175002 (2018)

초록

이 논문은 토로이달, 그리고 폴로이달 방향으로 대칭이며 토카막 바깥쪽으로의 입자 및 열 등의 수송에는 관여하지 않으나, 난류 수송을 억제시키는 zonal flow에 대한 연구에 관한 것이다. 이번 연구는 zonal flow 및 이의 shear의 특성 중 난류 억제 및 shear의 크기와 비충돌 조건에서의 토카막 기하 상에서의 잔여 값에 다룬다. 먼저 이온의 온도 기울기에 의해 유도되는 난류와 zonal flow의 shear의 토카막 안쪽과 바깥쪽의 비대칭성을 분석하고, zonal flow shear의 비대칭성이 난류의 억제에 미치는 영향에 대한 연구를 비선형 gyrokinetic 코드인 gKPSP를 활용한 시뮬레이션으로 수행하였다. $\mathrm{E}\times\mathrm{B}$ flow shear에 의한 난류 억제 이론에 근거한 분석 결과와 시뮬레이션 결과는 잘 일치하였으며, 비대칭적인 zonal flow의 shear가 난류를 대칭적으로 만든다는 것을 확인하였다. 이 $\mathrm{E}\times\mathrm{B}$ flow shear와 난류가 비대칭적인 것을 KSTAR의 ECEI data를 통해 다시 한번 확인하였고, 비대칭성의 정도를 시뮬레이션과 비교하였다. 마지막으로 Maxwellian 분포를 보이지 않는 고 에너지 입자가 zonal flow의 잔여 값에 미치는 영향에 대해 gyrokinetics와 bouncekinetics에 기반하여 체계적으로 유도하였다.

Keywords : 토카막 플라즈마, zonal flow, 안쪽과 바깥쪽간 비대칭성, 고에너지 이온, Gyrokinetics, ECEI

Student Number : 2013-23184

감사의 말

먼저 제가 박사 학위를 받을 때까지 저를 믿고 지원해주신 부모님과 동생에게 진심으로 감사의 말씀을 드립니다. 부족한 저에게 핵융합 플라즈마 이론 전반을 가르쳐주시고, 연구자로서의 마음가짐을 알려주신 제 지도 교수님 함택수 교수님이 있으셨기에 지금의 제가 있었습니다. 그 어떤 감사의 표현으로도 교수님께 받은 은혜를 보답할 수 없을 것입니다. 향후 연구자로서 교수님께서 지도해주신 바 마음 깊이 새기고 핵융합 플라즈마 분야에 이바지할 수 있도록 최선을 다하겠습니다. 저에게 뜻 깊은 조언을 해주신 황용석, 나용수, 정경재, 윤건수 교수님과 권재민 박사님께 감사드립니다. 그리고 제 학부시절부터 저에게 관심을 가져주시고 가르침을 주신 김곤호, 주한규 교수님께도 감사의 말을 전합니다. 비록 제자가 아니었으나, 연구에 벽을 맞이한 순간마다 저에게 도움을 주시고 길을 알려주신 장호건, 이수민 박사님께도 감사 드립니다.

같은 연구실에서 함께 배우고 연구해온 경진형, 경표, 병준, 용직에게 모두 격려와 감사의 말을 전합니다. 연구에 막힘이 있을 때마다 조언을 해주고 다른 힘든 일이 있을 때마다 도와준 연구실 선후배들이 있어 지금까지 면학에 힘쓸 수 있었습니다. 연구와 연구 외적으로도 저에게 다양한 조언을 해주신 동현형, 성무형, 상균에게 고맙다는 말을 전합니다. 이번 제 졸업 연구 주제 관련 연구를 함에 있어 도움을 준 상균, 영호와 포항 공대의 김동권 씨에게도 감사드립니다.

서울대학교에 입학하여 지난 10년간 동고동락을 함께 해온 10학번 모두 힘들 때마다 지탱해줘서 고맙다는 말을 전합니다. 공간이 부족하여 미쳐 다 적지 못하지만 저에게 도움을 주신 다른 많은 분들께 진심으로 감사의 말씀을 전합니다.